



# Thermal Modeling of an eVinci™-like heat pipe microreactor using OpenFOAM<sup>☆</sup>

Dean Price <sup>a,\*</sup>, Nathan Roskoff <sup>b</sup>, Majdi I. Radaideh <sup>a</sup>, Brendan Kochunas <sup>a</sup>

<sup>a</sup> Department of Nuclear Engineering and Radiological Science, University of Michigan, 2355 Bonisteel Blvd., Ann Arbor, MI 48109, United States of America

<sup>b</sup> Westinghouse Electric Company LLC, 1000 Westinghouse Dr, Cranberry Township, PA 16066, United States of America



## ARTICLE INFO

### Keywords:

eVinci™  
Microreactor  
Heat pipe  
OpenFOAM

## ABSTRACT

The simulation of heat pipe microreactors is an active area of research. In this paper, a thermal analysis of a heat pipe microreactor motivated by the eVinci™ design is performed. Thorough discussion on the modeling of heat pipes without a dedicated heat pipe modeling code, such as Sockeye, is also provided. The performance of two heat pipe modeling techniques is compared, one a more accurate approach which explicitly tracks heat pipe temperatures, and the other an approximation which simplifies the thermal hydraulic model development. One-way coupling is used where the Serpent neutronics code is used to generate a power distribution which is applied in an OpenFOAM model to calculate a temperature distribution. After a detailed convergence analysis, the core temperature distribution resulting from a core with control drums facing outward, or fully withdrawn, is compared with one having the control drums facing inward, or fully inserted. Finally, a parametric analysis was performed where the thermal resistances associated with the heat pipe model were varied and core temperatures were tracked. It was observed that the relationship between average and maximum core temperatures had a highly linear relationship to the thermal resistances used in the heat pipe model.

## 1. Introduction

Nuclear microreactors are defined in one reference as reactors whose power output is less than 20 MWe (Testoni et al., 2021). The motivation for these small-scale reactors is that they can address certain application areas where larger nuclear power plants, with much higher capital costs, would be prohibitively expensive. More specifically, one study (Black et al., 2022) lists five potential markets for electricity that could not be addressed by traditional large-scale nuclear power plants and would therefore be potential markets to demonstrate economic opportunities for microreactors. Briefly, these five potential markets are isolated markets, distributed energy, resilient urban, disaster relief and marine propulsion. The potential use cases for microreactors is further explored in Shropshire et al. (2021) where 11 use cases are proposed, categorized (according to the potential markets mentioned in Black et al. (2022)), and evaluated globally by region. Consistently across the globe, applications of microreactors in isolated operation had the largest market potential of the applications scenarios explored.

Spurred on by these economic opportunities a number of commercial entities are pursuing the development of microreactors as

listed in Testoni et al. (2021). Naturally, this has led to the development of simulation tools for the engineering analysis and design of microreactors. Although not specifically developed for microreactors, the Multiphysics Object Oriented Simulation Environment (MOOSE) has served as a platform for the development of these simulation tools (Lindsay et al., 2022). MOOSE enables the efficient development of application-specific programs, such as DireWolf (Matthews et al., 2021) which is used to perform multiphysics simulations for heat pipe microreactors. Recently, analysis on the heat pipe based eVinci™ microreactor (Swartz et al., 2021) was published where DireWolf was used to perform multiphysics simulations (Roskoff et al., 2022a,b). Steady-state, 2-group, neutron fluxes were displayed as calculated by Griffin (the neutronics solver in DireWolf) and the steady-state temperature distribution was also shown to peak at 1227 [K] in the fuel. In addition, accident-initiated transient simulations were performed for control drum initiated reactivity insertion accidents. Another multiphysics analysis of a heat pipe microreactor was performed where OpenFOAM and RMC are coupled to simulate the KRUSTY experiment (Poston, 2018) in order to demonstrate the capability of the

☆ ©2023 Westinghouse Electric Company LLC. All rights reserved.

\* Corresponding author.

E-mail address: [deanrp@umich.edu](mailto:deanrp@umich.edu) (D. Price).

their proposed methodology (Guo et al., 2022). Additionally, a multiphysics modeling analysis of a heat pipe microreactor incorporated stress analysis using OpenFOAM and ANLHTP (Jin Jeong et al., 2022) and the methodology was demonstrated on both a unit cell and full core model for transient calculations. An expansion of this work with neutronics coupling via PRAGMA was demonstrated on a steady-state problem where temperature, thermal expansion and core power were all calculated (Im et al., 2023). Alternatively, multiphysics calculations were performed with PROTEUS and SAM in the design process for the Holos-Quad microreactor (Stauff et al., 2022) which does not use heat pipes. The multiphysics simulation methodologies demonstrated in these papers all include neutronic feedback. In the current work, this feedback is not included, only thermal modeling is considered—which would be a portion of a full multiphysics coupling methodology which includes neutronics.

In general, many valuable studies have been published which demonstrate multiphysics modeling capabilities. These modeling capabilities are essential in the design and safety analysis of nuclear reactors but more detailed discussion on single physics modeling techniques specifically applied to microreactors—which are ultimately coupled to form the multiphysics simulation—could benefit from additional work. One paper (Mueller and Tsvetkov, 2021) presents a thorough discussion of the physical phenomena governing heat pipe operation as well as a range of modeling techniques that vary in complexity. The three modeling techniques explicitly implemented in the study demonstrated virtually identical results for steady-state calculations. One of the more simple modeling techniques discussed in the current work is presented in Zuo and Faghri (1998) where a network approach is used to quickly calculate heat pipe temperatures and heat flow characteristics. A more complex heat pipe model is used in the Sockeye code (Berry et al., 2019), which uses the two-phase flow model from RELAP-7 (Berry et al., 2018). Without heat pipes, standalone neutronic analysis for the Holos-Quad reactor was performed in the context of design optimization (Stauff et al., 2019). This current work seeks to perform an analysis specifically on heat transfer modeling of a heat pipe microreactor for efficient calculation of steady-state temperature distributions.

One-way coupling is a technique where either experimental or code-calculated data is integrated into a simulation without feedback. In Brockmeyer et al. (2020), one-way coupling is performed between a computational fluid dynamics software and structural models to analyze the effects of flow induced vibration on wire-wrapped fuel pins in sodium cooled reactors, and one-way coupling is used in Price and Kozlowski (2021) where experimental data on radial void fraction distributions are incorporated into neutronics models. In this work, one-way coupling is used by calculating pin power distributions with the Serpent (Leppänen et al., 2015) neutronics code and using them in the thermal model. The purpose of this work is not to obtain a converged multiphysics solution for engineering analysis but to use a somewhat realistic power distribution to assess numerical methods for steady-state thermal analysis. The results and discussion contained in this paper can be used to inform thermal modeling of heat pipe microreactors in the context of multiphysics simulation. Specifically, the impact of two methods for heat pipe modeling on the core temperature distribution is compared along with the temperature distributions arising from different control drum positions. Finally, a parametric sensitivity analysis is performed to evaluate the effect of heat pipe equivalent resistances on model results. The methods demonstrated in this paper can be used to inform thermal modeling procedures within a larger multiphysics modeling framework as is done in Price et al. (2023).

The remainder of this paper is organized with Section 2 providing the methods used in this work. It begins with a presentation on the design of the heat pipe microreactor modeled in this work in Section 2.1, followed by Section 2.2 describing the neutronics modeling required to obtain a fission power distribution. Section 2.3 discusses some

**Table 1**

Design parameters for EMD microreactor. All pitches are reported as the flat-to-flat distances for the hexagonal array.

Parameter	Value	Unit
Fuel Pin Diameter	1.7	[cm]
Pin Packing Fraction	40	[%]
Fuel Enrichment	19.75	[%]
Active Fuel Height	182	[cm]
Drum Liner Outer Radius	18.7	[cm]
Drum Liner Inner Radius	18.05	[cm]
Drum Liner Material	lead	NA
Drum B <sub>4</sub> C Coating Angle	110	[°]
Drum B <sub>4</sub> C Coating Thickness	1.5	[cm]
Drum Height	182	[cm]
Heat Pipe Outer Diameter	1.6	[cm]
Heat Pipe Wall Thickness	1.0	[mm]
Heat Pipe Material	SS304	NA
Shutdown Guide Tube Outer Radius	2.0	[cm]
Shutdown Guide Tube Thickness	0.3	[cm]
Shutdown Guide Tube Material	SS304	NA
Pin Cell Pitch	2.86	[cm]
Flake Pitch	18	[cm]
Reflector Outer Radius	120	[cm]
Container Height	280	[cm]
Container Outer Radius	130	[cm]
Container Thickness	10	[cm]

modeling details for the thermal modeling. Finally, Sections 2.4 and 2.5 are provided with discussion on how the heat pipes are modeled.

In Section 3, first the results from the Serpent calculations which yield fission power distributions are shown in Section 3.1. Then, a mesh-resolution analysis is presented in Section 3.2 to analyze the effect of different levels of modeling resolution on the temperature distribution results. This convergence analysis is followed by a temperature distribution comparison between two different core configurations, one configuration which has the control drums facing outward and one configuration which has the control drums facing inward in Section 3.3. The effectiveness of a heat pipe modeling approximation is discussed in Section 3.4. Finally, a parametric sensitivity study is presented in Section 3.5.

## 2. Methodology

### 2.1. An eVinci™-like heat pipe microreactor

In order to perform non-proprietary work that is still industry relevant, a heat pipe microreactor design was created that is similar to the eVinci™<sup>1</sup> microreactor currently under development at Westinghouse Electric Company. This proxy microreactor design is moderated by graphite, fueled using uranium oxycarbide TRISO particles, and controlled with 12 control drums. *It is referred to as the EMD (eVinci™ motivated design) microreactor from hereon out.* A labeled figure of the EMD microreactor core layout is provided in Fig. 1. The arrangement of fuel compacts and heat pipes within a fuel flake is shown in Fig. 2. Additional information pertaining to the design of the EMD is provided in Table 1. The tristructural isotropic (TRISO) particle geometries and materials used in these models follows the specifications provided in Electric Power Research Institute (2019) for the AGR-2 UCO TRISO particles. The core was designed to have a power output of 4 MWth with a core lifetime of 4 years and contains no burnable absorbers.

<sup>1</sup> eVinci is a trademark or registered trademark of Westinghouse Electric Company LLC, its affiliates and/or its subsidiaries in the United States of America and may be registered in other countries throughout the world. All rights reserved. Unauthorized use is strictly prohibited. Other names may be trademarks of their respective owners.

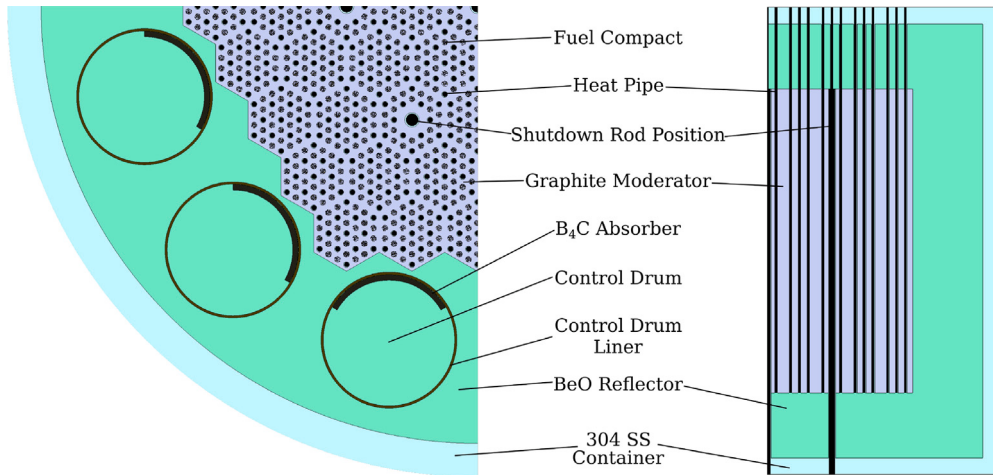


**Fig. 1.** Radial and axial diagram with labeled core components of EMD microreactor. Despite the 1/4 symmetry shown here, in neutronics modeling no symmetries are used.

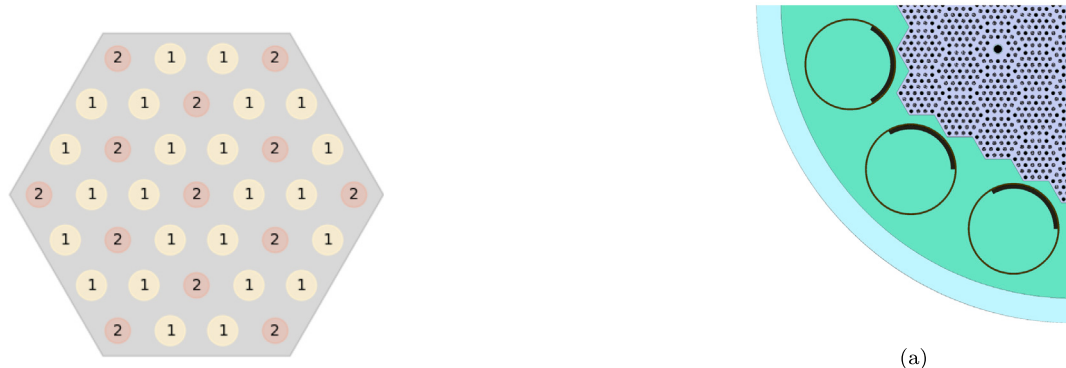
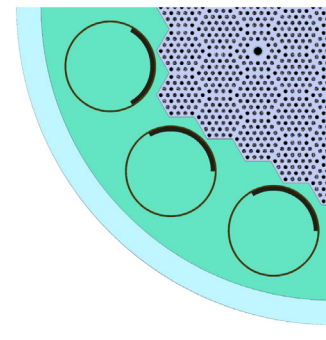


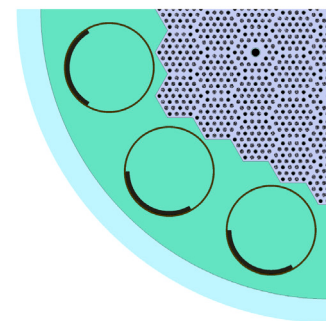
**Fig. 2.** Arrangement of fuel pins (positions labeled as "1") and heat pipes (positions labeled as "2") within the fuel flake. Fuel flakes that have shutdown rods have the center 7 positions replaced with a single shutdown rod guide tube.

## 2.2. Neutronics modeling

The Serpent 2 neutronics code (Leppänen et al., 2015) is used to generate pin power distributions to use in the OpenFOAM modeling framework. Serpent 2 is a continuous-energy Monte Carlo code used to solve the neutron transport equation for arbitrary 3D geometries. With the flexibility that comes with Monte Carlo codes, each spherical layer of the TRISO particles can be explicitly represented in the model without any homogenization. In this work, the pin power distributions are generated for fresh fuel both with the control drums facing fully inward and fully outward, as shown in Fig. 3. These two core configurations are used to analyze the thermal behavior of the core with two very different pin power distributions. The positions of these control drums have been shown to have a large effect on core power distributions in Price et al. (2022a). The outside surfaces of the microreactor are modeled with a vacuum boundary condition. The solution was obtained using 30,000 generations with 400,000 neutrons per generation and 50 inactive generations. In this neutronics model, the fuel and graphite was modeled at a spatially-uniform temperature of 1200 [K]. Furthermore, the Serpent model of this microreactor was modeled in 3D and pin power tallies were performed with 50 axial divisions and no symmetries. In order to obtain pin powers for the OpenFOAM model with 1/12 symmetry as used in thermal analysis, pin powers from the full model are mapped to their appropriate positions and averaged.



(a)



(b)

**Fig. 3.** Illustration of two model configurations, control drums in (a) and control drums out (b), used to generate pin power distributions.

## 2.3. Thermal modeling

An OpenFOAM-10 model of a 1/12 symmetry of the EMD microreactor is created to calculate heat flux and temperature distributions resulting from the Serpent-calculated pin power distributions. Heat pipes are modeled with boundary conditions as described in Section 2.4. The 1/12 symmetry is used to reduce the computational cost associated with generating results—all normal operational states of this microreactor should operate with this 1/12 symmetry so this assumption has no impact on results. The `chtMultiRegionFoam` solver is used for this analysis, it is capable of modeling multi-region

transient problems with both solid and fluid regions (Abbassi et al., 2020). In this application, only steady-state thermal diffusion through solids is required because there is no fluid movement in the parts of the microreactor which are being explicitly modeled in OpenFOAM. The semi-implicit method for pressure-linked equations (SIMPLE) algorithm is used to solve the steady-state heat transport equation using a pseudo-time stepping scheme (Patankar, 2018). The iterative procedure described in Section 2.4.1 for heat pipe modeling is integrated into the SIMPLE algorithm iterations such that the temperature fields and heat pipe parameters converge simultaneously. Alternatively, a more approximate method is presented in Section 2.4.2 that does not require direct intervention with the SIMPLE algorithm which leads to an easier implementation.

The OpenFOAM model is based on a 1/12 symmetry of the EMD microreactor with the absorbing region of the control drums replaced with BeO as they have minimal impact on thermal behavior. Additionally, perfect gap conductance between any material regions is assumed. Although this would lead to underestimates of overall core temperatures, it is used to avoid to the complexity of gap conductance modeling. Furthermore, all heat generation is contained within the fuel pin regions. Convection boundary conditions are used on the outsides of the stainless steel container with a temperature of 298 [K] and a convective heat transfer coefficient of 5 [W/m<sup>2</sup>-K]. An adiabatic boundary condition is used at the interface of the shutdown rod guide tubes and the graphite moderator. Due to symmetry, there are two surfaces which this boundary condition is applied to: (1) the interface between the graphite moderator and the center shutdown rod guide tube and (2) the interface between the graphite moderator and one noncentral shutdown rod guide tube. This approximation should be adequate, for steady state due to the large thermal resistance associated with these air-filled tubes. Meshing is performed with gmsh, an open source meshing software (Geuzaine and Remacle, 2009). The mesh is unstructured in the radial dimensions but is extruded in the z dimension and the fuel compact region is homogenized such that TRISO particles are not explicitly represented in the geometry. Furthermore, each fuel pin is divided into  $N_A$  axial segments and the power generation within each axial segment is constant. More discussion on the meshing strategy with a convergence study is presented in Section 3.2.1.

The fuel compact is comprised of 5 materials:

1. graphite
2. UCO fuel
3. Porous carbon
4. Pyrolytic carbon
5. Silicon carbide

A temperature-independent graphite thermal conductivity of 15 [W/m-K] based on 1200 [K] graphite as reported in Hollrah et al. (2022) is used solely for the fuel compact graphite. Also, a UCO thermal conductivity of 2.98 [W/m-K] is used based on the constitutive model contained in the BISON fuel performance modeling code (Hales et al., 2014) (model based on data from Nabielek et al. (1992)) for 1200 [K]. The thermal conductivities for the remainder of these materials is given in Stainsby et al. (2009) and the method included in Appendix C can be used to calculate the effective thermal conductivity (ETC) of the TRISO particle as 4.24 [W/m-K]. Four approaches for calculating the ETC of a homogenized fuel compact from the ETC of the particle are shown in Folsom et al. (2015) where the Chiew & Glandt model (Chiew and Glandt, 1983) with fitting parameters from Gonzo (2002) was deemed the most accurate compared to numerical modeling. Using this model, a constant thermal conductivity of 9.92 [W/m-K] is calculated for the ETC of the homogenized fuel compact. Following the method in Hollrah et al. (2022), the heat capacity of the compact is the mass-weighted average of its constituents. The thermal conductivity of the moderator graphite is modeled with a temperature-dependent fourth-order polynomial following the data presented in Hollrah et al. (2022).

## 2.4. Heat pipe boundary conditions

One objective of this work is to develop and assess the use of a simple heat pipe thermal circuit model that avoids the incorporation of dedicated heat pipe modeling codes into an analysis framework. These heat pipe models can be implemented as standard boundary conditions in any heat-transfer code by exploiting the convection boundary condition. Alternative heat pipe modeling methods which use boundary conditions to interface with the core temperature distribution solution method certainly exist. In Section III.A.3 of Matthews et al. (2021), two modeling options within the Sockeye heat pipe simulation tool are identified with a diagram given in Fig. 5 of that work. One modeling option includes a detailed two-phase flow model of the working fluid in the heat pipe while the other approximates the heat pipe as a solid thermal conductor. Both these methods use a 2-D-RZ representation of the heat pipe. The method demonstrated in the current work is more simple than both of these methods and can be classified as a lumped capacitance model according to the taxonomy provided in Mueller and Tsvetkov (2021).

To begin, the network approach for heat pipe modeling demonstrated in Zuo and Faghri (1998) will be used in this work. It was shown to provide accurate results, particularly for steady-state operating configurations. Another work (Hu et al., 2019) also used this network approach for steady-state modeling for verification of more complex transient-capable models and found all models agreed closely for steady-state. This network approach assumes that the temperature of the heat pipe vapor region is constant along its length. The validity of this assumption is also discussed in Mueller and Tsvetkov (2021) where it is stated that “in steady-state and most operating scenarios isothermal [in the vapor region] assumptions allow physics to be accurately captured”. Both studies use an additional assumption that is made in this paper where axial conduction in the heat pipe wall and wick are neglected. This is a reasonable assumption as the vast majority of axial heat transfer will occur in the vapor region for the physical system. The strength of the isothermal vapor core assumption is also demonstrated in Wang et al. (2017) where the axial vapor temperature distributions are shown to vary less than 1 K over the length of the heat pipe for multiple time steps during a startup transient. With these assumptions, Fig. 4 is provided to illustrate how the heat pipe is approximated using thermal circuits. Lastly, the operational limits of heat pipes will be ignored in this analysis. This is often where the complexity arises in existing heat pipe codes an inclusion of these operational limits may warrant the use of a dedicated heat pipe code.

In the OpenFOAM model, there is no explicit modeling of any part of the heat pipe. Instead, the physics of the heat pipe behavior is captured with the boundary condition which is imposed at the interface between the graphite moderator and the heat pipe. The interface between the heat pipe and the beryllium reflector is modeled as a zero heat flux interface as this would correspond to the adiabatic region of the heat pipe outer surface. With this, it is useful to relate the temperature of the heat pipe at the surface of the graphite moderator to the temperature of the vapor core of the heat pipe with

$$T_m(\mathbf{x}) = T_{vap} + r_1 q''(\mathbf{x}) \quad \mathbf{x} \in S. \quad (1)$$

In this expression,  $S$  is the 2-D domain on the surface of the graphite moderator in contact with the heat pipe,  $\mathbf{x}$  is a coordinate vector,  $T_m(\mathbf{x})$  is the temperature at the surface of the graphite,  $T_{vap}$  is the temperature of the heat pipe vapor core and  $q''(\mathbf{x})$  is the heat flux from the graphite moderator to the heat pipe at  $\mathbf{x}$ . Here,  $q''(\mathbf{x})$  is only defined in the region of the heat pipe that is within the active fuel region of the core. A representative thermal insulation between the moderator surface and the heat pipe vapor core is represented by  $r_1$ . This thermal insulation will be discussed in more detail in Section 2.5. Next, it is assumed that the temperature of the coolant on the outer surface of the condenser region of the heat pipe is held at a constant temperature. With this

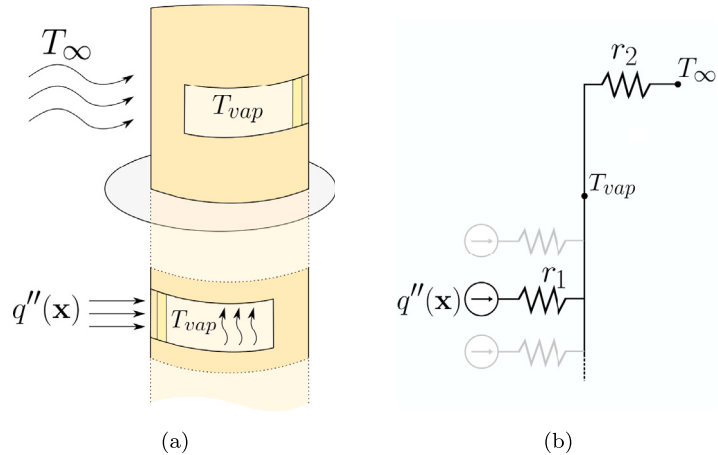


**Fig. 4.** Diagram of heat pipe (a) with cut-out regions in the evaporator and condenser regions to depict how some heat flux incident on the surface of the pipe at  $\mathbf{x}$  is transported out of the core. The representative thermal circuit (b) in terms of heat flux (as opposed to heat rate) approximates the heat transport behavior illustrated in (a) with two insulations,  $r_1$  and  $r_2$ . Additional heat flux sources which come from other parts of pipe not explicitly labeled in (a) are shown grayed out in (b).

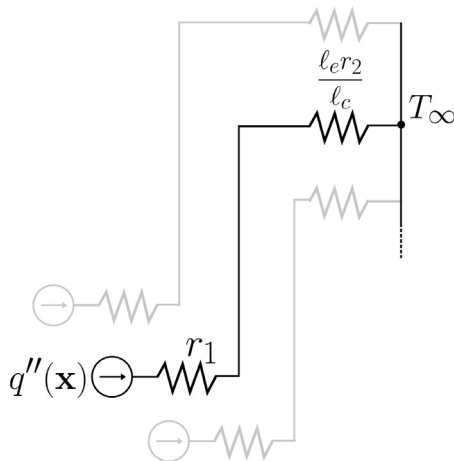


**Fig. 5.** Thermal circuit representation of LVTBC.

assumption, the temperature of the vapor region of the heat pipe can similarly be related to the temperature of the cooling fluid with

$$T_{vap} = r_2 q'' + T_\infty. \quad (2)$$

Here,  $T_\infty$  is used to represent the temperature of the cooling fluid in the heat exchanger and  $q''$  represents the uniform heat flux out of the outer surface of the heat pipe. In this work,  $T_\infty$  is a constant 791 [K] based roughly on the average of the inlet and outlet heat exchanger temperatures presented in Table IV of Gaspar et al. (2022). Similar to  $r_1$ ,  $r_2$  is a thermal insulance which represents any heat flow inhibitions between the external cooling fluid and the vapor core of the heat pipe. More discussion on this thermal insulance is also provided in Section 2.5. Also, in this relation there is no spatial dependence of any variables. Any heat transfer in the adiabatic region of the heat pipe is ignored. At steady state, the power out of the heat pipe in the condenser region and the power into the heat pipe in the evaporator region of the heat pipe is equal. Therefore, conservation of energy for a single heat pipe is

$$\int_S q''(\mathbf{x}) dS = \pi D \ell_c q''. \quad (3)$$

Here,  $D$  is the diameter of the outer surface of the heat pipe and  $\ell_c$  is the length of the heat pipe in the condenser region (assumed to be 1.82 [m]). The next two sections will detail how Eq. (1) and Eq. (2) can be used to derive boundary conditions for a heat transfer calculation.

#### 2.4.1. IVTBC: Iteration for $T_{vap}$

This boundary condition, referred to as iterative vapor temperature boundary condition (IVTBC), will involve iteratively solving for the temperature distribution in the core and then updating estimates for the heat pipe vapor temperatures ( $T_{vap}$ ). It is considered the more accurate of the two boundary conditions considered in this work. The thermal circuit which represents this solution strategy follows Fig. 4b. Each differential element on the boundary are connected in parallel, reconnecting before  $r_2$  such that all points on the boundary are coupled to form a constant  $T_{vap}$ . By solving Eq. (3), for  $q''_c$  and substituting into Eq. (2), the relation

$$T_{vap}^{(n,i)} = w \left( \frac{r_2}{\pi D \ell_c} \int_{S^{(n)}} q''^{(n,i)}(\mathbf{x}) dS^{(n)} + T_\infty \right) + (1 - w) T_{vap}^{(n,i-1)} \quad (4)$$

can be obtained. This equation introduces an iteration index  $i$  and a spatial index  $n$  for each heat pipe. The value of  $q''^{(n,i)}(\mathbf{x}) dS^{(n)}$  will come from the current estimate for the core temperature distribution. Here,  $S^{(n)}$  is the boundary of the graphite reflector in contact with the  $n$ th heat pipe,  $w$  is a relaxation factor and  $T_\infty$  is assumed to be constant across all heat pipes. This iterative method can be unstable so a relaxation factor of  $w < 1$  is often required for the solution method to converge. With some value for  $T_{vap}^{(n,i)}$ , a boundary condition of the form

$$q''^{(n,i+1)}(\mathbf{x}) = \frac{1}{r_1} \left( T_m^{(n,i+1)}(\mathbf{x}) - T_{vap}^{(n,i)} \right) \quad (5)$$

can be incorporated into many thermal modeling tools by repurposing the existing convection boundary condition. In this expression,  $T_m^{(n,i)}(\mathbf{x})$  is the temperature at the surface of the graphite in contact with the  $n$ th heat pipe on the  $i$ th iteration. Often the two inputs required by convection boundary conditions in common simulation tools are the temperature of the fluid external to the wall and the convective heat transfer coefficient. The numerical input for the convective heat transfer coefficient should be set to  $1/r_1$ . The numerical input for the temperature of the fluid external to the wall should be set to  $T_{vap}^{(n,i)}$ .

To initialize this iterative scheme, a spatially uniform  $q''^{(n,0)}(\mathbf{x})$  can be assumed such that

$$q''^{(n,0)}(\mathbf{x}) = \frac{P}{N \pi D \ell_e} \quad (6)$$

for all heat pipes. In this expression,  $P$  is the total reactor power,  $N$  is the total number of heat pipes and  $\ell_e$  is the length of the heat pipe in the evaporator region (i.e. heat pipe insertion depth into core). In this model,  $\ell_e = 1.82$  [m]. This leads to

$$T_{vap}^{(n,0)} = \frac{r_2 P}{N \pi D \ell_e} + T_\infty. \quad (7)$$

Algorithm 1 describes this solution scheme. A convergence criteria is established for this algorithm such that the maximum difference in the estimate for  $T_{vap}^{(n)}$  between consecutive iterations does not exceed  $\epsilon$ . After convergence is achieved, quantities of interest can be calculated from the thermal model with the converged boundary conditions.

**Algorithm 1** Iterative method for modeling heat pipe boundary condition.

```

for  $n \in \{1, 2, \dots, N\}$  do
     $T_{vap}^{(n,0)} \leftarrow \frac{r_2 P}{N \pi D \ell_c} + T_\infty$ 
end for
 $i \leftarrow 1$ 
while  $\max \left\{ \left| T_{vap}^{(n,i)} - T_{vap}^{(n,i-1)} \right| ; n = 1, 2, \dots, N \right\} > \epsilon$  do
    Solve heat equations with  $T_{vap}^{(n,i-1)}$  as boundary conditions as
    described in Equation (5)
    for  $n \in \{1, 2, \dots, N\}$  do
        Extract  $\int_{S^{(n)}} q''^{(n,i)}(\mathbf{x}) dS^{(n)}$  from solution to heat equations
         $T_{vap}^{(n,i)} \leftarrow w \left( \frac{r_2}{\pi D \ell_c} \int_{S^{(n)}} q''^{(n,i)}(\mathbf{x}) dS^{(n)} + T_\infty \right) + (1-w) T_{vap}^{(n,i-1)}$ 
    end for
     $i \leftarrow i + 1$ 
end while
```

One additional method can be used to more efficiently acquire accurate solutions. The SIMPLE solution method used in OpenFOAM to converge on a spatial temperature distribution is also iterative. One strategy for obtaining optimal performance is to update the heat pipe vapor temperatures before satisfactory temperature distributions are achieved within the SIMPLE solution method. This update takes the form of changing boundary conditions as described in (5). In this way, an “inner iteration” for each iteration of the SIMPLE algorithm and an “outer iteration” for each heat pipe vapor temperature update can be formed. The result from the inclusion of these inner iterations is that the heat pipe vapor temperatures and core temperature distribution converge simultaneously.

#### 2.4.2. LVTBC: Non-iterative approximation

The boundary condition described in Section 2.4.1 can be cumbersome to implement as it requires a separate programmatic infrastructure which can solve for the temperature field in the model multiple times and update the vapor temperature in each heat pipe. Therefore, it may be convenient to formulate a boundary condition which does not rely on any iterative method (external to the thermal modeling software) and can be easily implemented as a convective boundary condition. This convenience can be gained by making the assumption that a local approximation for  $q_c$  can be obtained using

$$\tilde{q}_c(\mathbf{x}) \approx \frac{\ell_e}{\ell_c} q''(\mathbf{x}). \quad (8)$$

This approximation is “local” because the estimation of  $q_c$  will vary depending on  $\mathbf{x}$  and is not physically motivated. The ratio of  $\frac{\ell_e}{\ell_c}$  is required to account for different heat transfer areas in the evaporator or condenser regions. Instead, it is practically motivated as it circumvents the need to explicitly calculate and update heat pipe vapor temperatures. Hence, a functional dependence of  $\mathbf{x}$  is introduced and a tilde is used to indicate that this is an approximation of  $q_c$ . This approximation is exact if  $q''(\mathbf{x})$  is constant along the outer surface of the heat pipe. Nevertheless, this approximation can be substituted into Eq. (2) to obtain

$$T_{vap} \approx \frac{r_2 \ell_e}{\ell_c} q''(\mathbf{x}) + T_\infty. \quad (9)$$

Then, Eq. (9) can be substituted into Eq. (1) to obtain

$$q''(\mathbf{x}) \approx \left( \frac{r_2 \ell_e}{\ell_c} + r_1 \right)^{-1} (T_m(\mathbf{x}) - T_\infty). \quad (10)$$

This boundary condition will be referred to as the local vapor temperature boundary condition (LVTBC). The thermal circuit shown in Fig. 5

is included to illustrate the differences between IVTBC and LVTBC. For LVTBC, there is no coupling across elements on the boundary. Instead, each element is linked to  $T_\infty$  with two thermal insulations in series. This differs from the thermal circuit used for IVTBC (shown in Fig. 4b) because a uniform  $T_{vap}$  is not enforced for the heat flux across all boundary elements. Similar to the boundary condition presented in the previous section, this boundary condition can be incorporated using the convection boundary conditions which are standard in any heat transfer modeling software. The numerical input for the convective heat transfer coefficient should be set to  $\left( \frac{r_2 \ell_e}{\ell_c} + r_1 \right)^{-1}$ . The numerical input for the temperature of the fluid external to the wall should be set to  $T_\infty$ . One additional point of comparison between IVTBC and LVTBC is that they become identical if  $r_2 = 0$ . This can be seen by setting  $r_2 = 0$  in Eq. (2) such that  $T_{vap} = T_\infty$ . Then, Eq. (5), pertaining to IVTBC, and Eq. (10), pertaining to LVTBC are identical. Of course, this condition would also remove the need for iteration in the context of IVTBC.

#### 2.5. Thermal insulation approximations

As mentioned previously,  $r_1$  and  $r_2$  are thermal insulations which represent the constriction of heat flow into and out of the vapor core, respectively. The conventional definition of a resistor in a thermal circuit,  $R$ , is that it describes the change in temperature per unit heat rate across the thermal insulator. Here the thermal insulation,  $r$ , is the change in temperature per unit heat flux across the thermal insulator. Following the description of the thermal circuit model provided in Hu et al. (2019),  $r_1$  is the summation of four separate insulations:

1.  $r_{1a}$ : Insulation due to contact resistance between the graphite moderator and the heat pipe wall.
2.  $r_b$ : Insulation due to heat propagation through heat pipe outer wall.
3.  $r_c$ : Insulation due to heat propagation through heat pipe wick.
4.  $r_d$ : Insulation due to interface resistance between the heat pipe wick and vapor core.

Similarly for  $r_2$ :

1.  $r_{2a}$ : Insulation due to convective heat transfer between the heat pipe outer wall and cooling fluid in heat exchanger.
2.  $r_b, r_c$  and  $r_d$ : Retain their meanings from their introduction in the context of  $r_1$ .

Some approximate values will be assigned to these insulations in this section. However, in Section 3.5, the sensitivity of core temperatures to these insulations will be explored to determine the effect that these approximate insulation values may have on the results.

Nevertheless,  $r_{1a}$  will be the first parameter to be addressed and it is equal to the inverse of the interfacial conductance,  $h_{1a}$ , between the graphite moderator and stainless steel heat pipe

$$r_{1a} = \frac{1}{h_{1a}}. \quad (11)$$

The interfacial conductance for the stainless steel, graphite contact would be a difficult parameter to estimate for this work as it would be highly dependent on the contact characteristics between the graphite and the stainless steel wall of the heat pipe (pressure, surface finish, etc.). Therefore, a value of  $h_{1a} = 800$  [W/m<sup>2</sup>-K] will be used such that  $r_{1a} = 1.25 \times 10^{-3}$  [m<sup>2</sup>K/W]. Next,  $r_{2a}$  can be described using the convective heat transfer coefficient between the surface of the heat pipe in the condenser region of the heat pipe and the coolant in the heat exchanger as

$$r_{2a} = \frac{1}{h_{2a}} \quad (12)$$

From experimental data collected from the eBlock37 microreactor demonstration unit (Gaspar et al., 2022), an approximate value of  $h_{2a} = 307$  [W/m<sup>2</sup>-K] was determined. The corresponding  $r_{2a} = 3.26 \times 10^{-3}$

**Table 2**  
Thermal insulances for heat pipe boundary condition calculation.

Quantity	Approximate value [m <sup>2</sup> K/W]
$r_{1a}$	0.00125
$r_{2a}$	0.00326
$r_b$	$5.34 \times 10^{-5}$
$r_c$	$2.48 \times 10^{-5}$
$r_d$	$5.15 \times 10^{-7}$
$r_1$	0.00133
$r_2$	0.00334

[m<sup>2</sup>K/W] will be used here. The insulation for the interface between the heat pipe wick and vapor core can be described in terms of a heat transfer coefficient and a geometry adjustment factor

$$r_d = \frac{1}{h_d} \frac{D}{D - 2t_{wall} - 2t_{wick}} \quad (13)$$

Here,  $t_{wall}$  is the heat pipe wall thickness and  $t_{wick}$  is the thickness of the heat pipe wick and will be taken from Gaspar et al. (2022) to be 0.36 [mm]. A value for  $h_d$  is taken directly from Hu et al. (2019) as  $2.34 \times 10^6$  [W/m<sup>2</sup>-K]. Again, these estimated values should be considered to have high uncertainty. The effect of which is explored in Section 3.5.

The thermal conductivity ( $k_{wall}$ ) and thickness of the heat pipe wall can be used to describe  $r_b$  as

$$r_b = \frac{D \ln \left( \frac{D}{D-2t_{wall}} \right)}{2k_{wall}}. \quad (14)$$

Similarly for  $r_c$ , where and  $k_{wick}$  is an equivalent thermal conductivity of the wick,

$$r_c = \frac{D \ln \left( \frac{D-2t_{wall}}{D-2t_{wall}-2t_{wick}} \right)}{2k_{wick}}. \quad (15)$$

A value of  $k_{wall} = 20$  [W/m<sup>2</sup>-K] is used based on experimental results from Sweet et al. (1987) and an approximate value of  $k_{wick} = 17$  [W/m<sup>2</sup>-K] is used based on the eBlock37 microreactor demonstration unit (Gaspar et al., 2022). With these specifications, Table 2 provides numerical values for the insulances presented in this section. From this table, the values for  $r_1$  and  $r_2$  are largely determined by  $r_{1a}$  and  $r_{2a}$ , respectively—this is consistent with the observations in Panda et al. (2017).

### 3. Results

#### 3.1. Pin power distributions

In order to obtain realistic pin power distributions to incorporate into the thermal model, Serpent 2 is used for two core configurations, one with the control drums facing inward and one with the control drums facing outward. The Serpent calculation was run with 50 axial tally divisions in each pin and the power results are shown in Fig. 6. In postprocessing, the pin powers from the full Serpent model (with no symmetries) are mapped to their positions as if the calculations were run with 1/12 symmetry, this has no effect on the results other than reducing the uncertainty due to the Monte Carlo calculation method in these results. These figures show both the radial and axial power distributions where the lines representing the axial power distribution of each pin are colored according to its total pin power.

There are some clear trends in the axial power shapes calculated for both core configurations. The power increases sharply at the ends, around -75 [cm] and 75 [cm], of the active fuel region due to the increased moderation provided by the BeO reflector outside of the axial fuel region. This effect is more pronounced in the case where control drums are facing inwards because the absorbing region of the control drums only occupy the active fuel region. Therefore, the flux depression

from the control drums has a smaller effect in the axial reflector. Aside from this, the typical cosine-shape is biased towards the bottom of the core. This is due to the presence of the stainless steel heat pipes extending through the reflector on the top region of the core and not to bottom region as shown in Fig. 1. These heat pipes will absorb neutrons in this upper reflector region and suppress the neutron flux.

Also, the radial pin power distribution is different for the two cases. First, the pin power distribution resulting from the core with drums facing inward has clear center-peaking behavior where the highest power pins are in the center of the core. The radial power distribution from the core with drums facing outward has a comparatively flatter radial power shape with a low power region midway between the center and outside of the core. The power is higher in the edges of the core for the same reason as the power increases in upper and lower regions of the pin as shown in the axial power distributions—the moderation from the BeO reflector. Naturally, a realistic operating configuration for this reactor will have the control drums partially withdrawn. As such, these pin power distributions represent more extreme core power shapes than would typically be expected. In order to incorporate these pin power distributions into the thermal models, each axial distribution is fit with an 8-th degree polynomial (and rescaled to preserve the total power) which is then integrated within each of the  $N_A$  axial segments to obtain the constant region powers required for the OpenFOAM model.

#### 3.2. Convergence analysis

##### 3.2.1. Mesh convergence

In order to ensure that accurate results are obtained from the thermal modeling, it is useful to perform a mesh convergence study. This study uses the pin power distribution shown in Fig. 6b where the control drums are facing outward with IVTBC. To maintain a reasonable computational cost, a constant axial power is assumed such that  $N_A = 1$ , the impact of this assumption on calculation results will be shown in Section 3.3. The results from this mesh convergence study with the maximum core temperature and maximum heat pipe vapor temperature across all heat pipes as comparative metrics are shown in Table 3. These maximum temperatures are used as convergence metrics, not necessarily accurate representations of maximum temperatures given that  $N_A = 1$ . In this table, the characteristic mesh length (CML) is a general indicator of the edge length of the mesh used to solve the heat equation. Another quantity,  $CML/r_{pin}$  is the CML divided by the radius of the fuel pin which is included to provide some indication of how finely the unstructured mesh can capture the curvature of the fuel pin. Regardless of the mesh size used in this exploration, the coarsest representation of the pin is as a hexagonal prism. For  $CML/r_{pin} \leq 1$ , the geometry of the pin is more accurately represented with a prism with more sides. In the axial direction, the mesh is extruded with segments roughly  $3 \times CML$  to reduce mesh resolution in this direction. The reflector and container are also modeled with coarser meshes. From these results, the comparative metrics remain relatively unchanged across the CML sizes used, with a maximum core temperature only ranging about 13 [K]. To maintain brevity, pictures and additional discussion of the various mesh sizes are included in Appendix. For the remainder of the results shown in this paper, a mesh with  $CML = 0.6$  [cm] is used. Although this may lead to errors in maximum or minimum temperatures, this selection is unlikely to affect the qualitative convergence characteristics of the methods shown.

##### 3.2.2. SIMPLE algorithm with IVTBC

In order to solve for the temperature distribution in the core using IVTBC, an iterative procedure is required where the core temperature distribution is calculated for some set of heat pipe vapor temperatures, then, the heat pipe vapor temperatures are updated. The procedure for performing this iterative solution method is discussed in Section 2.4.1. In order to evaluate the stability of this solution approach, a set of

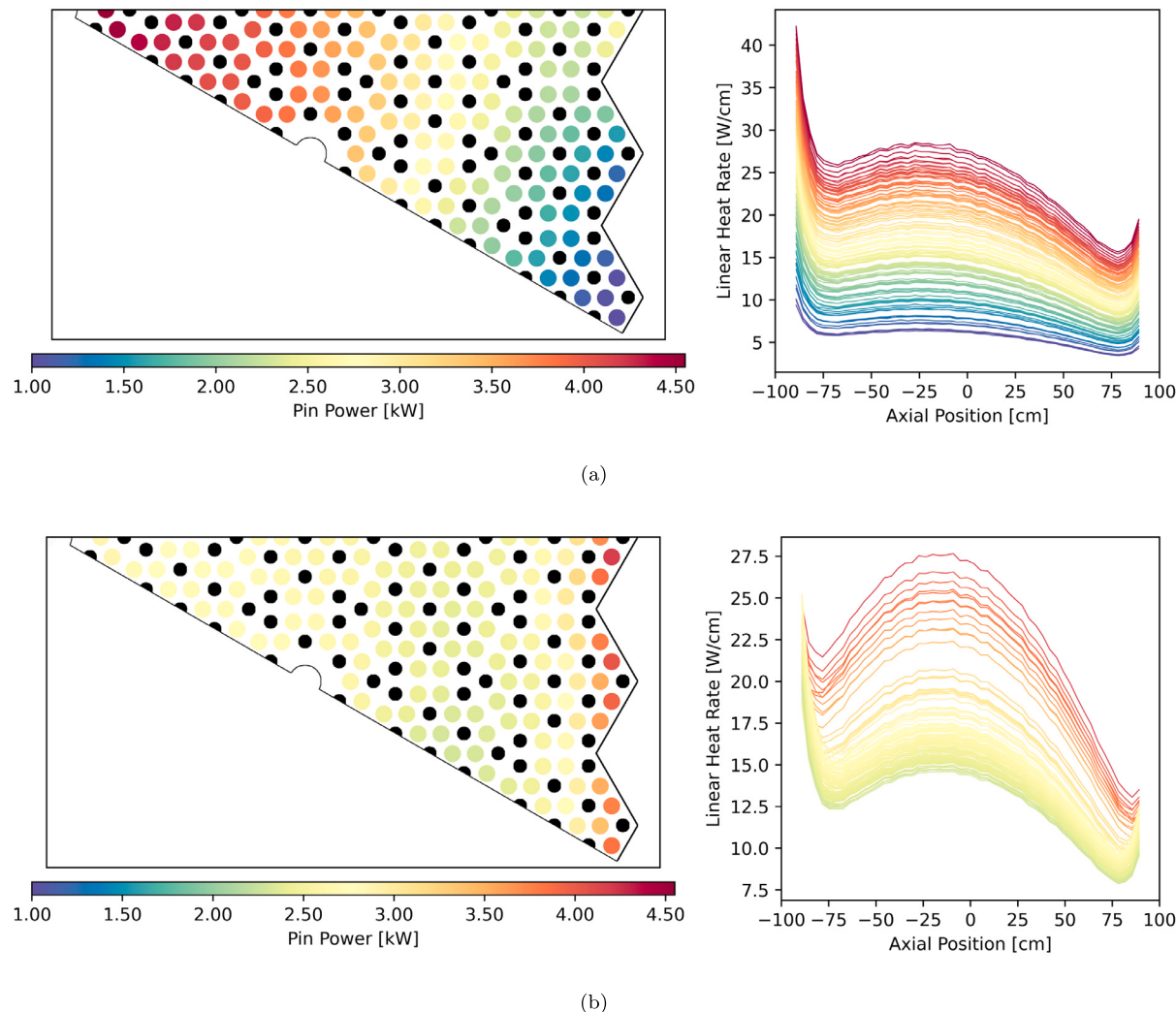


**Fig. 6.** Serpent-calculated radial and axial power distributions for EMD microreactor with control drums facing inward (a) and control drums facing outward (b). The axial power distributions keep the color of their position in the radial power distribution plot.

**Table 3**

Values of maximum core temperature and maximum heat pipe vapor temperature for different levels of mesh resolution.

CML [cm]	CML/ $r_{pin}$	Cells [million]	Core $T_{max}$ [K]	Heat pipe vapor $T_{max}$ [K]
2	2.5	0.222	1118.1	956.8
1	1.3	0.468	1111.0	957.8
0.8	1.0	1.39	1111.5	959.1
0.6	0.75	1.96	1109.4	957.8
0.4	0.50	7.13	1105.1	958.0

calculations is run on the EMD OpenFOAM model. For these calculations,  $CML = 0.6$  cm, 6 axial divisions are used ( $N_A = 6$ ) and 200 initial iterations of the SIMPLE algorithm are run before beginning to update heat pipe vapor temperatures. With the solution method described in Algorithm 1, there are two algorithm parameters which must be selected:

- $w$ : the relaxation factor used in the outer iteration to update the heat pipe vapor temperatures as given in Eq. (4).
- update interval (int.): number of inner iterations used to solve the 3D conduction equation before initiating the heat pipe vapor temperature update routine.

As  $w$  is used to increase algorithm stability, it should be between 0 and 1. Fig. 7 shows the convergence behavior for four different calculations run with different  $w$  and int. for a calculation run with the control drums facing outward. On the left portion of Fig. 7, the vapor

temperatures for each of the 75 heat pipes is shown as a function of total inner iterations. Each of the four plots in the left portion of Fig. 7 correspond to an individual calculation. In the right portion of Fig. 7, the relative power residual is plotted for each of the four calculations. The relative power residual is defined as

$$\text{Rel. Power Residual} = \left| \frac{\text{Total Power out of core}}{4 \text{ MW}/12} - 1 \right|. \quad (16)$$

The “Total Power out of core” is calculated with the surface-integrated heat flux out of all outer surfaces of the core model—including outer container surfaces. The denominator in this expression is the total heat generated in the 1/12 model of the core. In this figure, “x” marks are given at the iteration numbers where the heat pipe vapor temperatures are updated. Calculations with a higher number of intervals between vapor temperature updates (int.) will have fewer updates for a fixed number of total inner iterations.

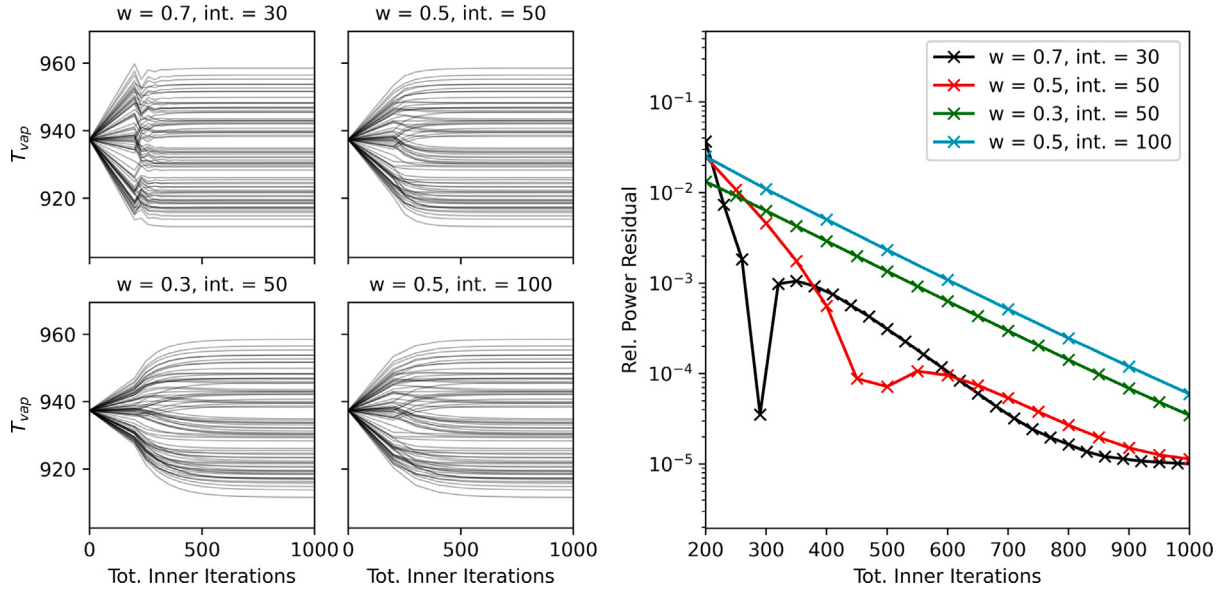


**Fig. 7.** Convergence information for four calculations run with different algorithm parameters applied to the EMD model with control drums facing outward. The left portion of the figure shows the evolution of  $T_{vap}$  across each of the 75 heat pipes where each line corresponds to the temperature of a heat pipe. The right portion of the figure shows an indicator of the overall temperature convergence using the metric given in Eq. (16).

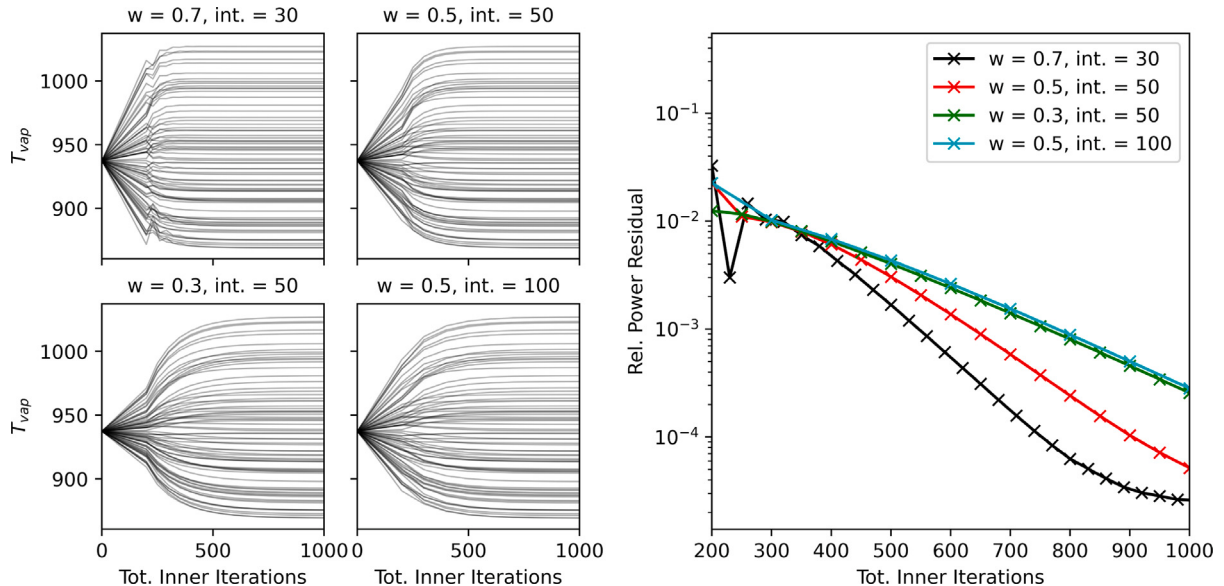


**Fig. 8.** Convergence information for four calculations run with different algorithm parameters applied to the EMD model with control drums facing inward with same format as Fig. 7.

From the results shown in Fig. 7, the calculation with  $w = 0.7$  and  $\text{int.} = 30$  is included to show how instabilities can develop in the solution scheme. These instabilities are caused by the heat pipe vapor temperature change responding to an insufficiently converged temperature distribution in the graphite region. In this specific case, the oscillations seen in the heat pipe vapor temperatures decay away to yield fully converged solutions, but this is not guaranteed. Selecting a lower  $w$  and higher  $\text{int.}$  tends to yield a more stable solution algorithm as these oscillations are damped by sufficiently converging the temperature distribution before making an update to the heat pipe vapor temperatures. By comparing the two calculations run with  $\text{int.} = 50$ , it is clear that a higher  $w$  leads to a more efficient solution because the relative power residual decreases much faster for the calculation run with  $w = 0.5$  than for the calculation run with  $w = 0.3$ . Similarly,

the two calculations where  $w = 0.5$  can be compared to observe that selecting a lower  $\text{int.}$  leads to faster convergence. All four of these calculations converged to the same values of  $T_{vap}$  for each pipe. Similar conclusions can be seen in Fig. 8 where the same calculations were run but with a power distribution representing the core with drums facing inward. Overall, the calculations run with  $w = 0.5$  and  $\text{int.} = 50$  seem to demonstrate similar convergence speed to the calculations run with  $w = 0.7$  and  $\text{int.} = 30$  but without any oscillation.

### 3.2.3. SIMPLE algorithm with LVTBC

Regardless of the convergence rate of these calculations, IVTBC requires a small amount of additional time to update the heat pipe vapor temperatures which is not accounted for here. Nevertheless, the purpose of this section is to compare the convergence rate of

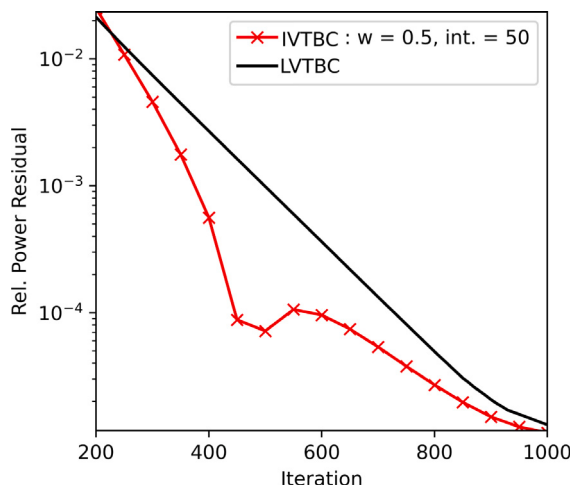


Fig. 9. Convergence behavior of a calculation with IVTBC with  $w = 0.5$  and int. = 50 and a calculation with LVTBC.

calculations run with IVTBC to those run with LVTBC. Fig. 9 shows the relative power residual for a calculation of IVTBC with  $w = 0.5$  and int. = 50 and LVTBC. LVTBC does not require any heat pipe vapor temperature updates so it does not have any algorithmic parameters associated with it. Despite the results showing that IVTBC converges faster than LVTBC, there is currently no theoretical support that this is generally the case. Instead, these results should suggest that the use of IVTBC may not impede the convergence of the temperature distribution as compared to LVTBC.

### 3.2.4. Axial power divisions

As mentioned in Section 2.3, each pin in the OpenFOAM model must be divided into  $N_A$  axial regions with constant powers in each region. At the time of writing this, with the current publicly-available versions of OpenFOAM, heterogeneous power within a region is not yet supported. With this software limitation, it is important to analyze the effect that the number of axial divisions has on the temperature solution. Therefore, a set of 8 calculations were performed using IVTBC and the associated procedure described in Algorithm 1 with  $\epsilon = 1$  [K]. Each of these 8 calculations has a value for  $N_A$  ranging from  $N_A = 1$  to  $N_A = 25$ . The power for each axial division in each pin was calculated using the pin power distributions for the core with the control drums facing inward as shown in Fig. 3b.

Fig. 10 shows the centerline temperature of the fuel pin located at  $x = 7.1$  [cm] and  $y = -2.5$  [cm] (origin at core center) for each of the 8 calculations. The region-wise constant linear heat rate is also shown on each of these figures, the y-axis limits on this quantity are deliberately selected to show the close match between the shape of the region-wise linear heat rate and the resulting temperature distribution. The temperature distributions corresponding to the calculations run with  $N_A \leq 8$  tend to reflect the stepwise constant behavior of the linear heat rate. As heat flux is proportional to the gradient of the temperature distribution, this stepwise behavior indicates that there is little axial heat flow in the pin within an axial division. Instead, all heat is flowing in the radial direction—directly towards the heat pipe. For calculations with higher  $N_A$ , the temperature distribution tends to be smoother. Furthermore, due to the sharp power peaks at the upper and lower boundaries caused by reflector thermalization, the maximum centerline temperature occurs near the bottom of the pin. The location of this peak is resolved for higher values of  $N_A$ , being reasonably approximated for calculations with  $N_A \geq 14$ .

In fact, the maximum temperature within a pin is an important quantity for safety analyses as it can indicate thermal limit violations. For further exploration on the effect of  $N_A$  on pin-wise maximum

temperatures, Fig. 11 shows the evolution of the maximum temperature for each of the 123 total pins in the model as  $N_A$  increases. The maximum change in maximum fuel temperature between the model with  $N_A = 1$  and  $N_A = 25$  is 39 [K]. When comparing models with  $N_A = 2$  and  $N_A = 25$ , this maximum change goes down to 22 [K]. This inaccuracy can be significant, when maximum temperatures are quantities of interest, a higher degree of resolution in capturing axial power distributions is important. On the other hand, Fig. 11 also shows that pinwise average temperatures change very little across models with different  $N_A$ . The maximum change in average fuel temperature between the model with  $N_A = 1$  and  $N_A = 25$  is 5.7 [K]. Similarly, the change in heat pipe vapor temperatures for each of the 75 heat pipes across different values of  $N_A$  is shown in Fig. 12. In these results the maximum change in vapor temperatures is 3.8 [K]. Contrary to the conclusion regarding maximum fuel temperatures, when averaged quantities are the primary focus, it is less important to capture the axial power shape with high resolution. A similar conclusion can be made about calculating heat pipe vapor temperatures as these temperatures are essentially the result of an integrated heat flux along the heat pipe boundary. These conclusions suggest that heat-pipe microreactor design efforts pertaining to the analysis of heat pipes specifically can be performed with 2D models.

### 3.3. Power distribution results comparison

Fig. 6 shows that two reactor configurations, one with control drums facing inward and one with control drums facing outward, can significantly impact the pin power distributions for the microreactor. In Fig. 13, the resulting radial temperature distributions at the core midplane from the two pin power distributions are shown. For these calculations, IVTBC is used with  $N_A = 6$  and  $\epsilon = 1$  [K]. There is a significant difference between these two temperature distributions as well. The temperature distribution resulting from the pin powers calculated with the control drums facing outward is much flatter, with a hotter reflector region. As expected, the more significant radial peaking shown in Fig. 6 for the pin power distribution from control drums in carries over to the temperature distribution as well. Furthermore, the hottest region of the core from the case calculated with control drums facing inward is the core center where it is the outer edge of the fueled region in the case calculated with control drums facing outward. These general trends carry over to the heat pipe power distributions shown in Fig. 14. In this figure, the total power removed from the core by each heat pipe is shown for both control drum positions. The range in heat pipe powers for the calculation with control drums facing inward is significant, the heat pipes near the center of the core remove twice the heat as those at the periphery of the fueled region. This is highly undesirable behavior as heat pipes have operational limits at both high and low powers. However, it is also highly unlikely that the core would ever run at a significant power with control drums facing inward as it would be difficult to achieve criticality. This observation is likely valid for any microreactor design as a core designed to operate at beginning of life with all control drums in would have an insufficient shutdown margin.

### 3.4. Boundary condition results comparison

In the fast-moving domain of microreactor design and analysis, it may be desirable to avoid the extra work required to implement IVTBC into an analysis framework. In these scenarios, LVTBC may be a reasonable alternative. To compare the results from IVTBC and LVTBC, radial temperature distributions at core midplane are given in Fig. 15, and the axial temperature distributions are given in Fig. 16. At the core midplane, LVTBC tends to yield higher temperatures than IVTBC and therefore more conservative results. This is because local estimations of the heat pipe vapor temperatures, from Eq. (9), are based on the heat flux at a particular point on the boundary. Therefore, hotter parts

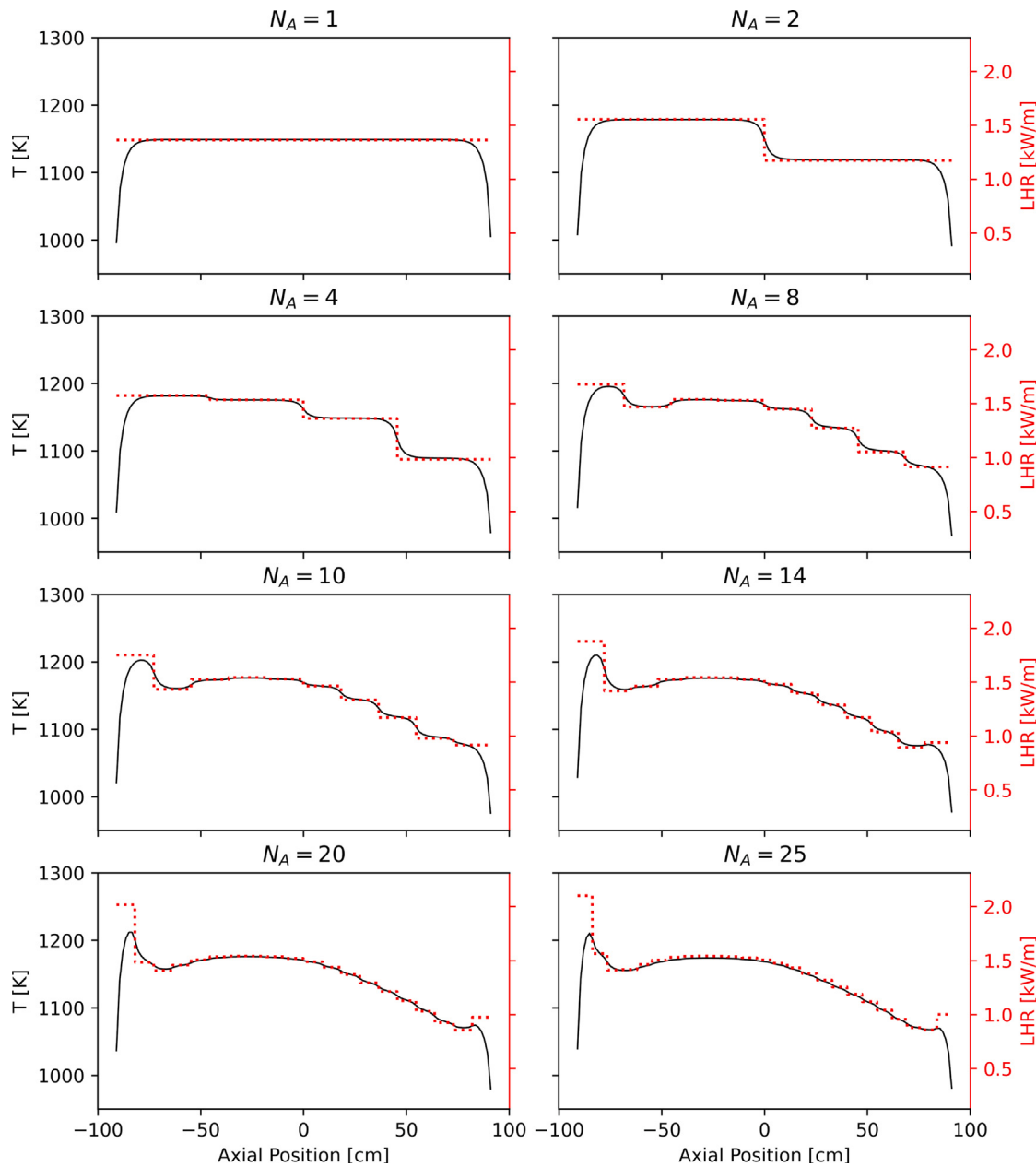


**Fig. 10.** Centerline fuel temperature for fuel pin located at  $x = 7.1$  [cm] and  $y = -2.5$  [cm] (origin at core center). Linear heat rates used in each axial division also included for reference.

of the core will tend to overestimate heat pipe vapor temperatures—compared to IVTBC—leading to higher comparative temperatures. On the other hand, IVTBC tends to diminish the thermal peaking behavior as the superconductivity of the heat pipes will “spread out” the heat in the core. This also leads to colder regions of the core in LVTBC having lower temperatures than those regions in IVTBC. At the extremes, LVTBC can overestimate the temperature by 75 [K] in the middle region of the core and underestimate the temperature by 19 [K] in the upper region of the core. Overall, LVTBC does an insufficient job in capturing the core temperature distribution from this analysis. However, in other analyses, LVTBC may be sufficient as IVTBC and LVTBC become identical as  $r_2$  goes to 0.

### 3.5. Insulation parametric study

In Section 2.5, approximate values for  $r_1$ , the representative thermal insulance between the heat pipe boundary and heat pipe vapor core,

and  $r_2$ , the representative thermal insulance between the heat pipe vapor core and the heat exchanger cooling fluid are presented. As these approximate values are subject to high uncertainties, it is important to quantify the impact that these model parameters have on results. Without precise uncertainty bounds, a bounding analysis is used where the variation of reactor parameters is analyzed over a very large range of values for  $r_1$  and  $r_2$ . In Fig. 17 the results of a parametric sensitivity study are presented. For one set of calculations,  $r_1$  is varied over 8 logarithmically-spaced points while  $r_2$  is kept at its reference value of 0.00334 [ $\text{m}^2\text{K}/\text{W}$ ]. Then, maximum fuel temperature, average fuel temperature, maximum moderator temperature and average moderator temperature are calculated for each value of  $r_1$ . For another set of calculations, a similar procedure is used by varying  $r_2$  with  $r_1$  kept at its reference value of 0.00133 [ $\text{m}^2\text{K}/\text{W}$ ]. The range of variation of these parameters does not necessarily represent their uncertainty.

Overall, the relationship between both  $r_1$  and  $r_2$  to these temperatures is highly linear. Table 4 is given to show the slope of a line

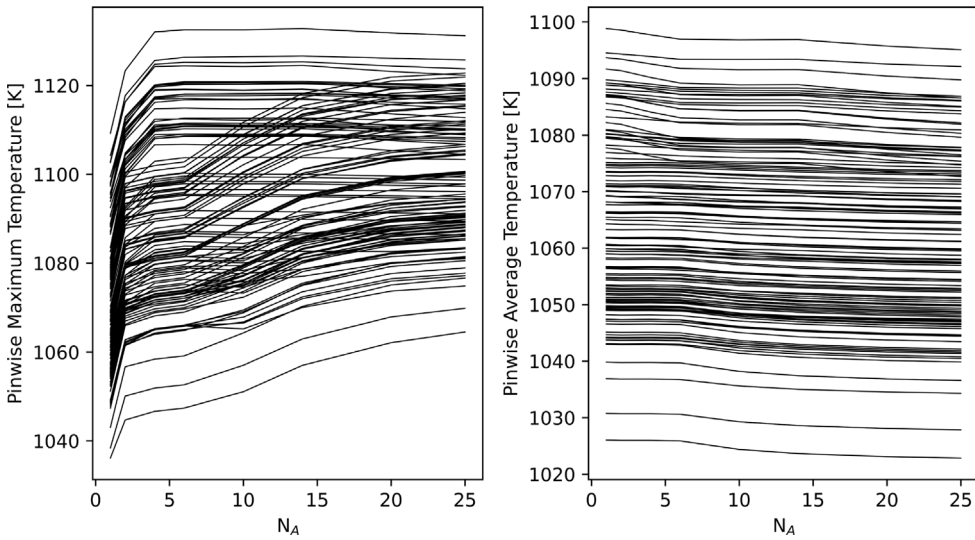


**Fig. 11.** Maximum and average fuel pin temperatures for each of the 123 total pins from models with varying  $N_A$ .

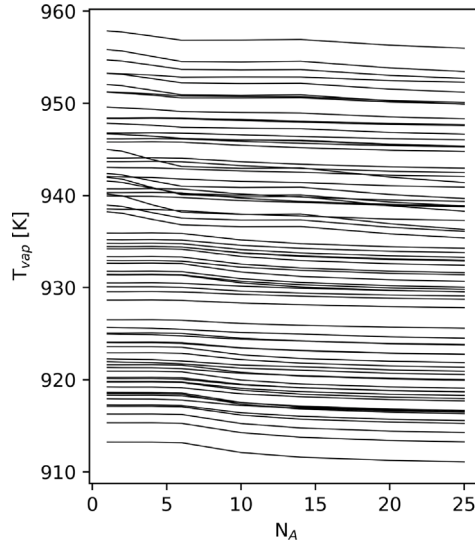


**Fig. 12.** Heat pipe vapor temperatures for each of the 75 heat pipes from models with varying  $N_A$ .

fitted to these data points, the coefficient of determination for all fitted lines is very high ( $R^2 > 0.999$ ). For these models, this linearity is expected because the material properties were mostly taken to be constants. Therefore, any scaling or shifting of the boundary heat flux should simply scale or shift the temperature distribution similarly. The graphite thermal conductivity—the one material property which changes with temperature—seems to have little effect on this linearity. Although the values of sensitivity measures shown in Table 4 are higher for the results pertaining to  $r_1$  than  $r_2$ , the uncertainty ranges for  $r_1$  and  $r_2$  should be taken into account before asserting that the variation in a particular parameter is more impactful on the final results than another. With uncertainties, a formal sensitivity analysis can be performed using linear models as shown in Price et al. (2022b). Nevertheless, the sensitivity measures pertaining to the maximum temperatures are similar within  $r_1$  and  $r_2$ . This is due simply to the similarity in the values of the maximum fuel temperature and maximum moderator temperature as shown in Fig. 17 where the maximum fuel temperature

is consistently about 15 [K] over the maximum moderator temperature. Similar observations can be made about the sensitivity measures pertaining to the average temperatures. Overall, these results suggest that effort should be taken to quantify the uncertainties associated with  $r_1$  and  $r_2$  because they can have a significant effect on core temperatures. However, this effect can likely be quantified with a simple 1-point perturbation approach due to the linearity in the relationship between these insulations and core temperatures.

#### 4. Conclusions

This work has presented results from a thermal model of a heat pipe microreactor which explicitly models the effect of the heat pipes on core temperature distributions using a thermal network model. The convergence of the model results for different levels of modeling resolution was analyzed. It was found that capturing the axial variation in pin powers was not entirely necessary if average temperatures were of interest. However, maximum temperatures are inaccurate for low resolutions of the axial pin power distribution. The effect of an alternative, approximate, method for modeling heat pipes is also explored and found to be insufficient for the current microreactor model. The effect of two different Serpent-calculated pin power distributions on core temperatures are also analyzed. One pin power distribution was calculated with the control drums facing inward and the other was calculated with the control drums facing outward. Significantly different temperature distributions were observed, as expected, with a wider range of temperature variation found in the temperature distribution corresponding to control drums facing inward. Finally, the sensitivities of maximum and average core temperatures to changes in heat pipe modeling parameters were quantified. More specifically, the thermal insulation representing the inhibition of heat flow from the core reflector to the heat pipe vapor core and the thermal insulation representing the inhibition of heat flow from the heat pipe vapor core to the cooling fluid in the heat exchanger were the quantities of interest. A strong linear relationship was observed between core temperatures and these insulations. As these thermal insulations have large uncertainties because they are dependent on contact properties between moderator and heat pipe, more work should be undertaken to quantify and reduce these uncertainties. Overall, the methods presented in this work do not include neutronics or fuel performance as is done in Matthews et al. (2021) but is intended to be a more detailed exploration of thermal modeling procedures for a heat pipe microreactor.

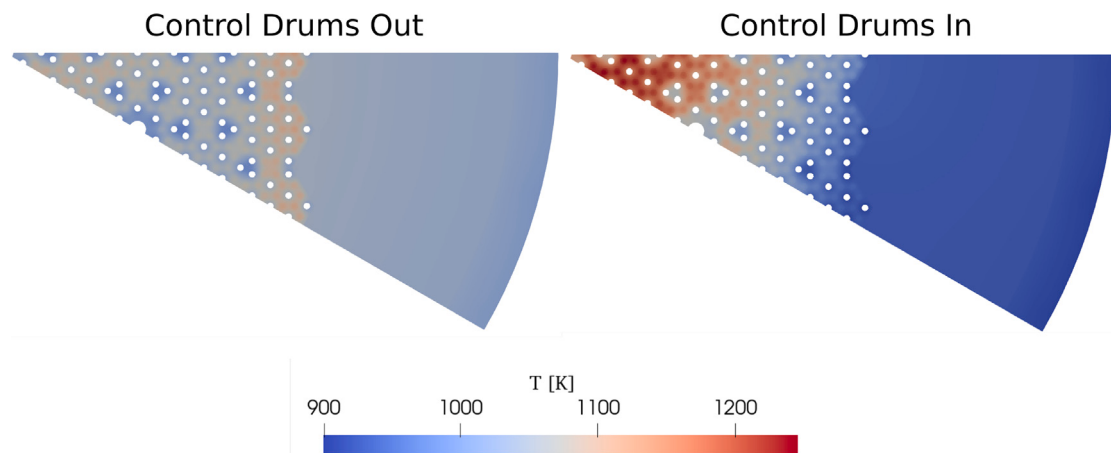


Fig. 13. Radial temperature distribution taken at core midplane from the two core power distributions calculated with control drums facing inward and outward.

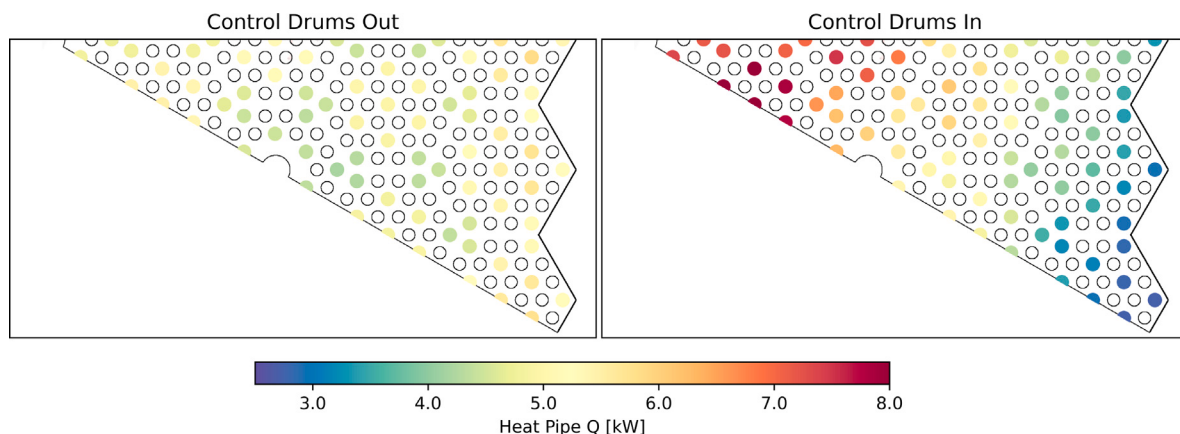


Fig. 14. Power taken out of core by each heat pipe for two core power distributions calculated with control drums facing inward and outward.

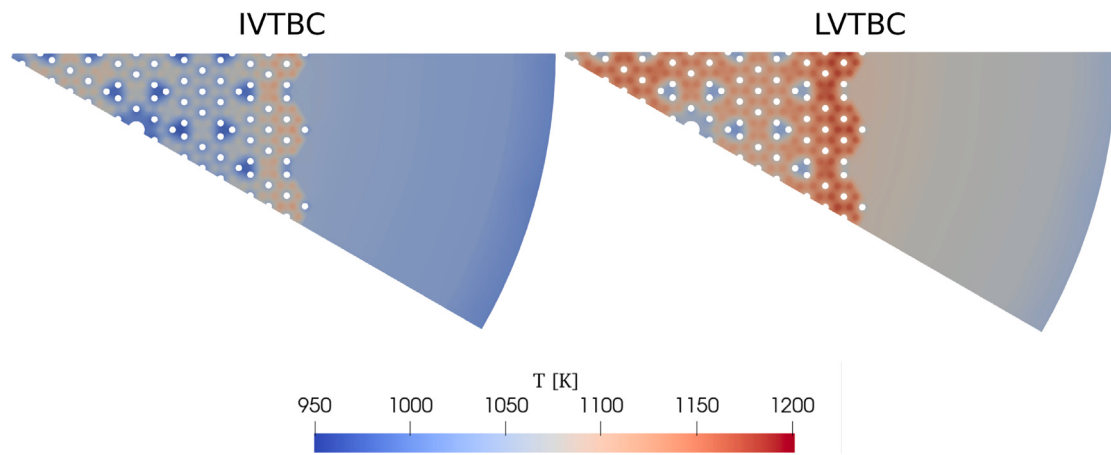
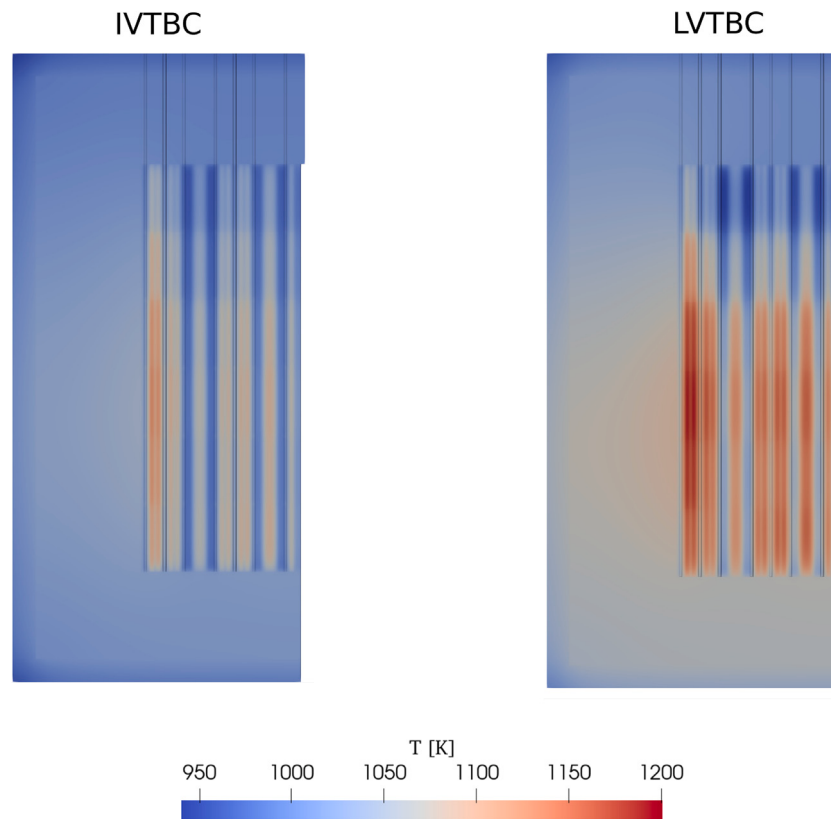


Fig. 15. Radial temperature distributions at core midplane for IVTBC and LVTBC.

**Table 4**  
Sensitivity measures for the response of core temperatures to variations in  $r_1$  and  $r_2$ .

$T_i$	$\Delta T_i / \Delta r_1$ [kW/m <sup>2</sup> ]	$\Delta T_i / \Delta r_2$ [kW/m <sup>2</sup> ]
Maximum Fuel Temperature	63.5	42.4
Average Fuel Temperature	53.6	41.2
Maximum Moderator Temperature	63.7	42.3
Average Moderator Temperature	53.5	41.5



**Fig. 16.** Axial temperature distributions for IVTBC and LVTBC.

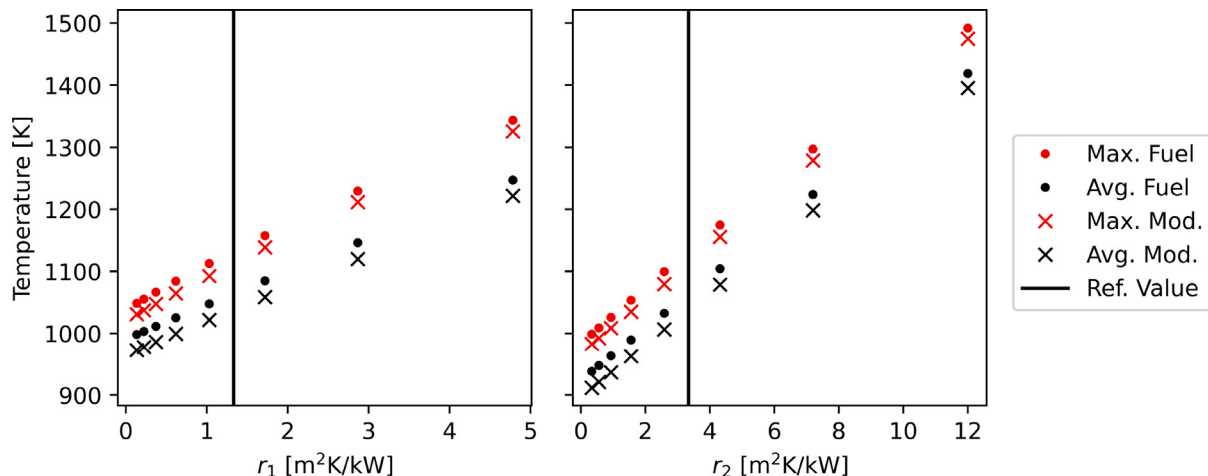


**Fig. 17.** Core temperatures for different values of  $r_1$  and  $r_2$ .

#### CRediT authorship contribution statement

**Dean Price:** Conceptualization, Methodology, Software, Formal analysis, Investigation, Writing – original draft, Visualization. **Nathan Roskoff:** Conceptualization, Methodology, Validation, Resources, Writing – review & editing, Supervision, Project administration. **Majdi I. Radaideh:** Methodology, Writing – review & editing, Supervision. **Brendan Kochunas:** Conceptualization, Resources, Writing – review & editing, Supervision, Project administration.

#### Declaration of competing interest

The authors declare that they have no known competing financial interests or personal relationships that could have appeared to influence the work reported in this paper.

#### Data availability

The authors do not have permission to share data.

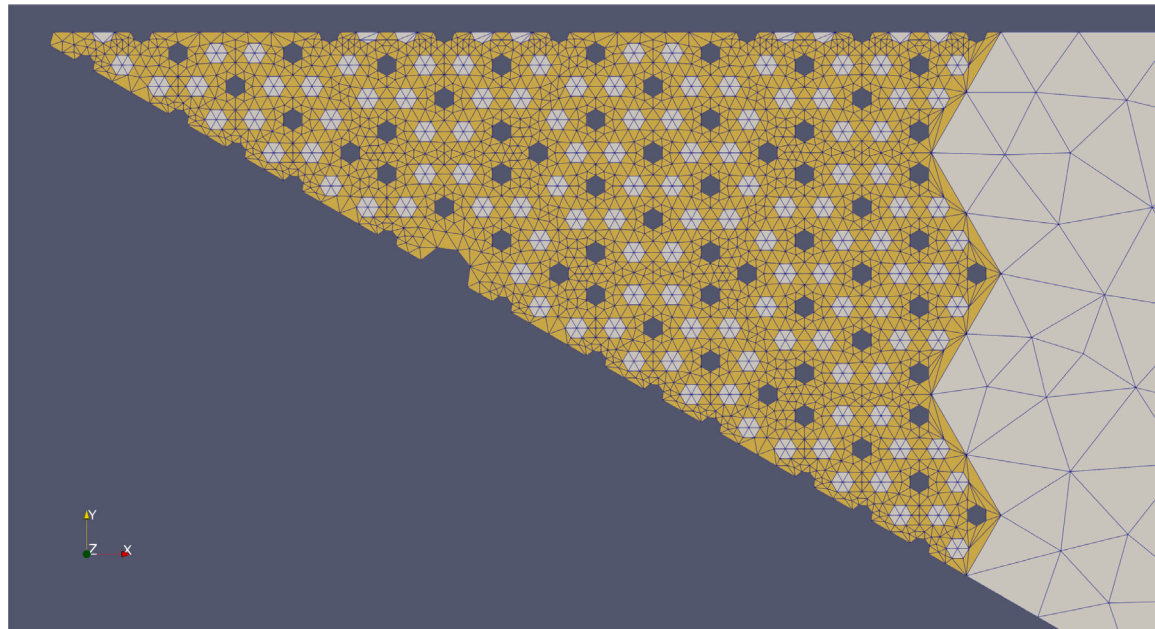
## Acknowledgments

We would first like to thank Cole Mueller for his valuable correspondence in the early stages of this work. This material is based on work supported under a Department of Energy, Office of Nuclear Energy, United States of America, Integrated University Program Graduate Fellowship, United States of America. This research made use of Idaho National Laboratory computing resources which are supported by the Office of Nuclear Energy, United States of America of the U.S.

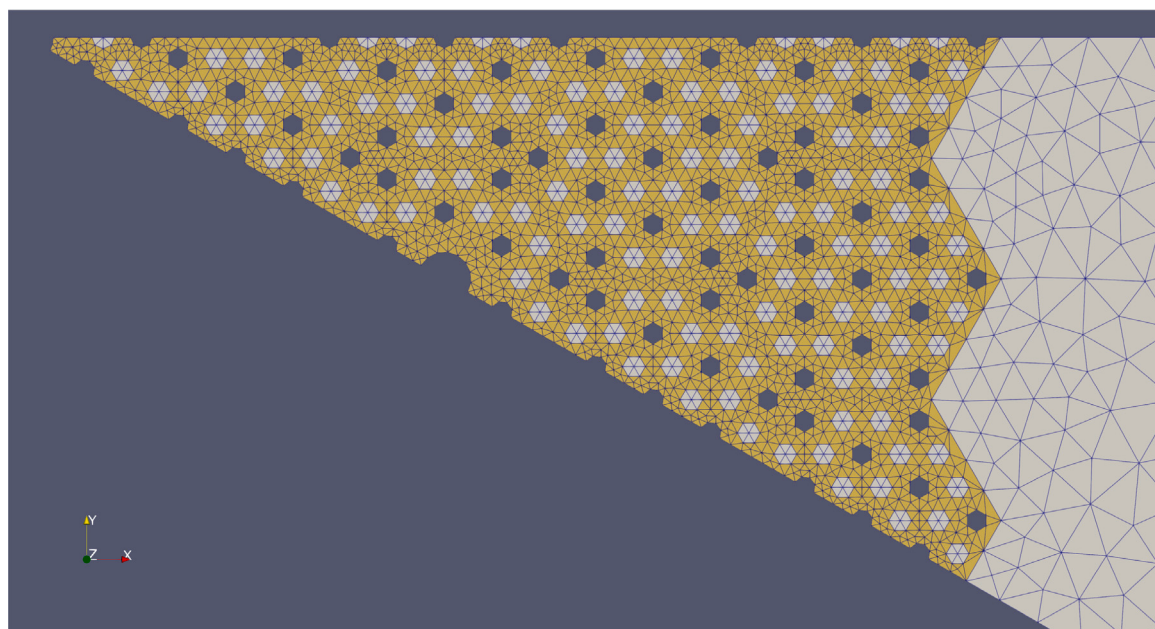
Department of Energy and the Nuclear Science User Facilities, United States of America under Contract No. DE-AC07-05ID14517.

## Appendix. Mesh convergence analysis figures

In Section 3.2.1, some discussion and comparative metrics were given for the thermal model of the EMD with different mesh sizes. To supplement this section, some illustrations of the meshes are supplied

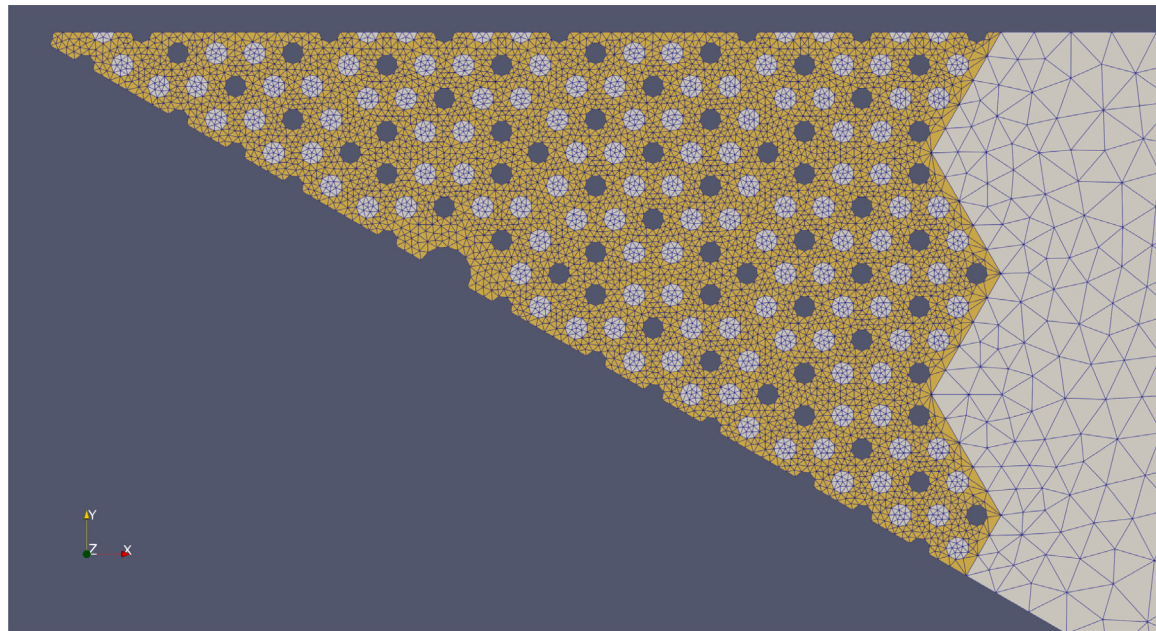


(a) CML = 2 cm

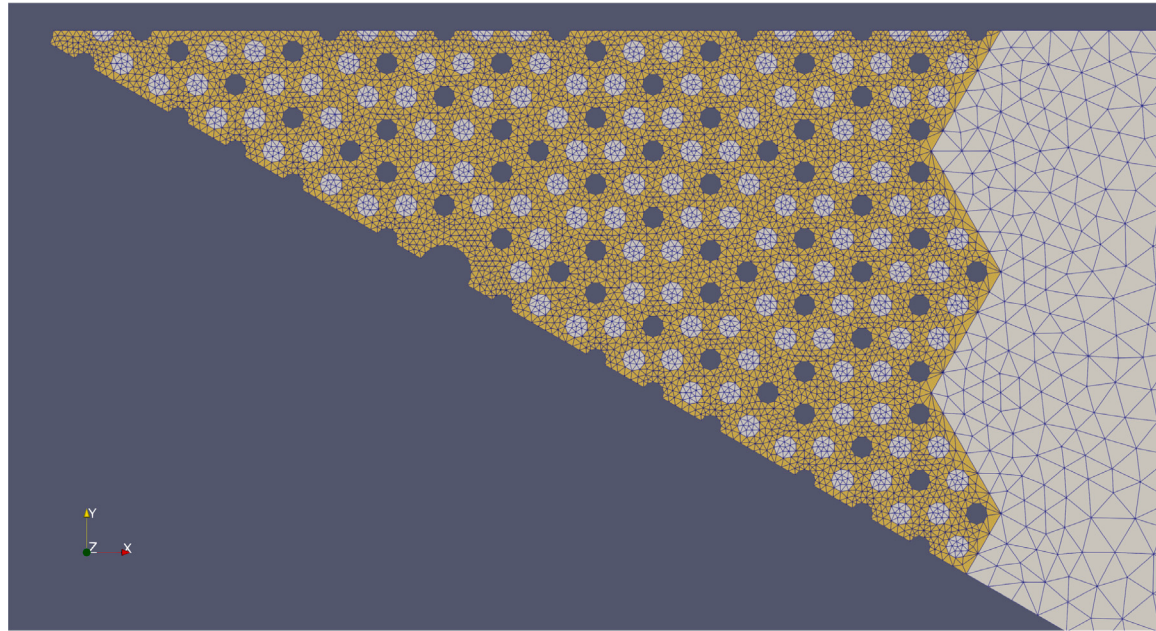


(b) CML = 1 cm

**Fig. A.18.** Radial mesh for 5 different resolutions shown as a cross-cut at core centerline.



(c) CML = 0.8 cm

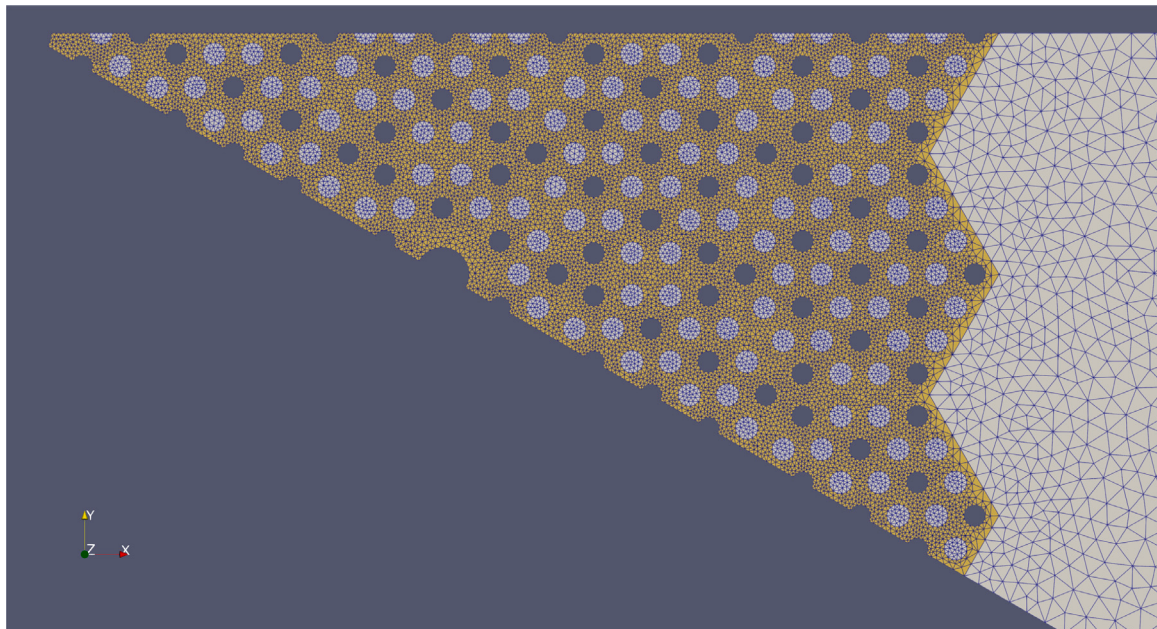


(d) CML = 0.6 cm

Fig. A.18. (continued).

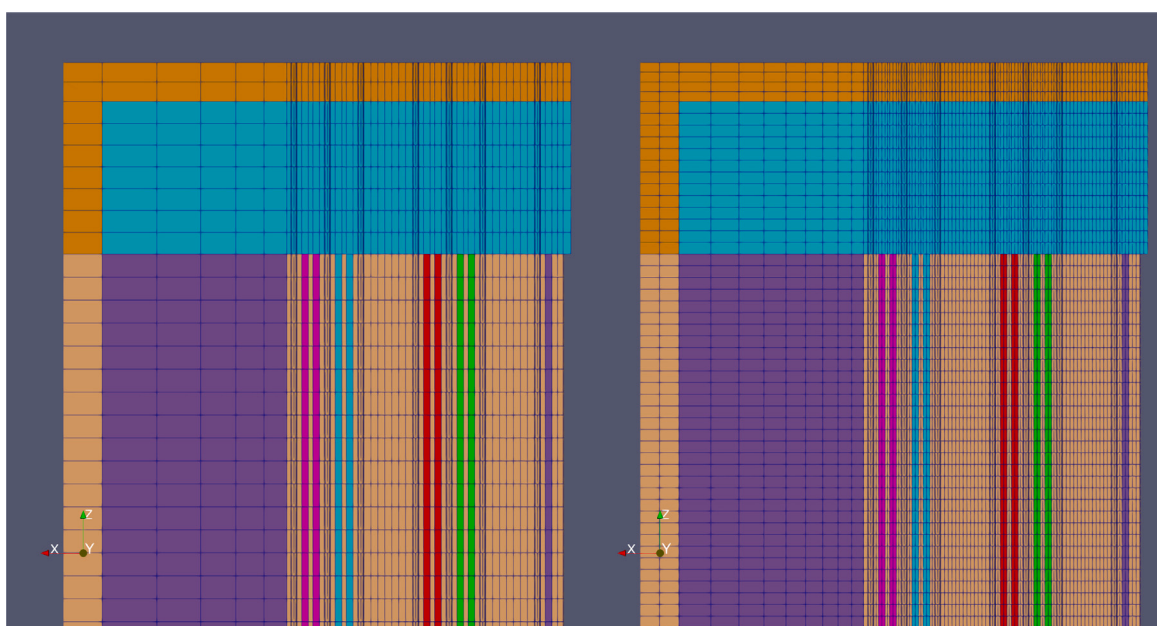
in the current section. The radial mesh for 5 different levels of mesh resolution is shown in Fig. A.18. In this figure, the two coarser meshes (CML = 2 and CML = 1) represent each cylindrical pin as a hexagonal prism. For lower CML values, the shape of the pins is captured more accurately with more mesh elements. Furthermore, the differences in mesh resolution in the fueled region of the core and the reflector are

shown in these figures. The graphite moderator is shown in yellow with a finer mesh than the reflector which is shown on the right side of these figures in gray. The resolution of the mesh in the axial direction is shown in Fig. A.19. Being an extruded mesh, the radial mesh at each axial level is identical. The distance between axial divisions gets smaller as the CML decreases.



(e) CML = 0.4 cm

Fig. A.18. (continued).



(a) CML = 2 cm

(b) CML = 1 cm

Fig. A.19. Axial mesh for 5 different resolutions shown for top half of model.

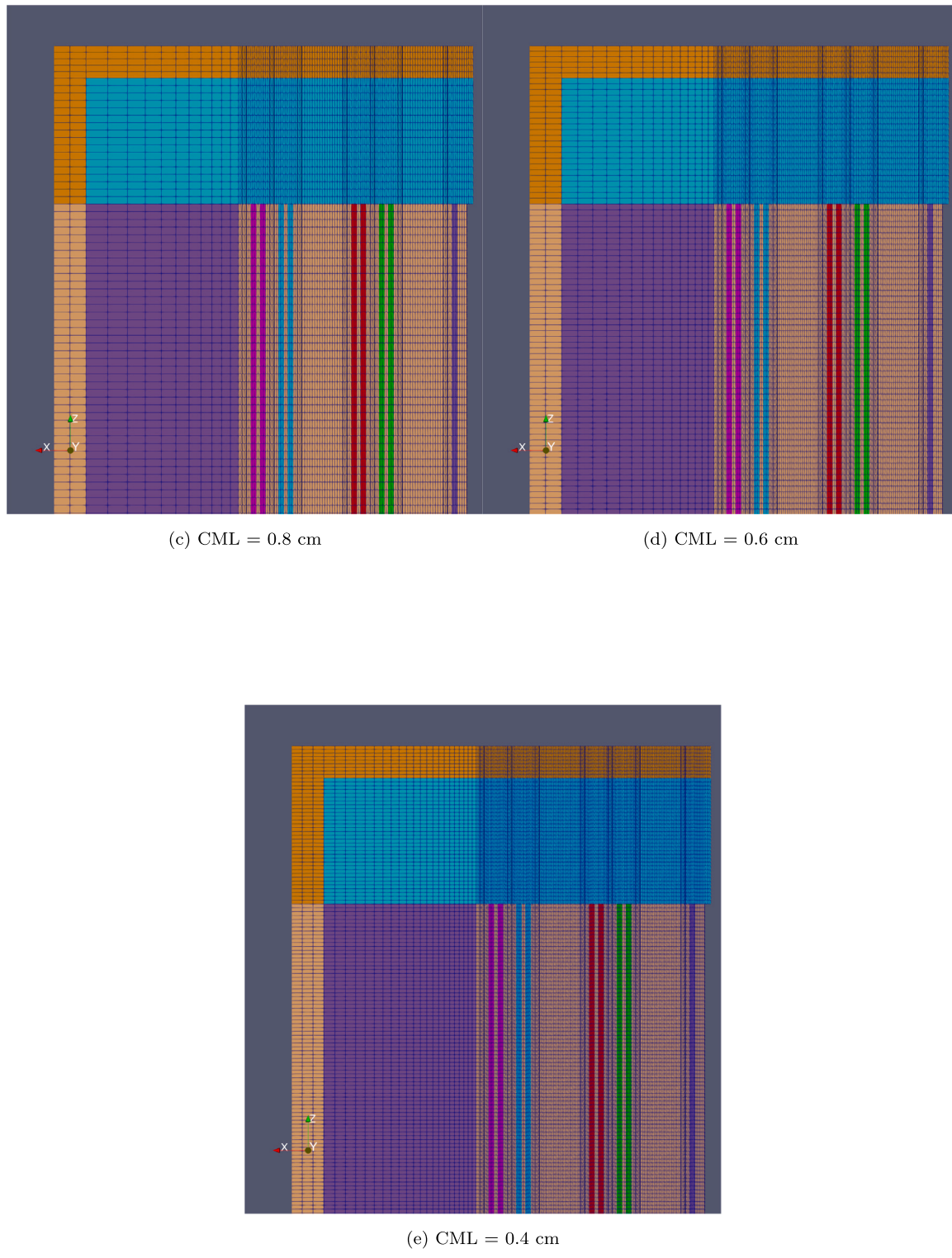


Fig. A.19. (continued).

## References

- Abbassi, M.e., Lahaye, D., Vuik, K., 2020. Modelling turbulent combustion coupled with conjugate heat transfer in openfoam. In: Numerical Mathematics and Advanced Applications ENUMATH 2019: European Conference, Egmond aan Zee, the Netherlands, September 30–October 4. Springer, pp. 1137–1145.
- Berry, R.A., Kunick, M., Andrs, D., Hansel, J.E., Martineau, R.C., 2019. Sockeye heat pipe code theory development: Based on the 7-equation, two-phase flow model of RELAP-7. Tech. rep., Idaho National Lab.(INL), Idaho Falls, ID (United States).
- Berry, R.A., Peterson, J.W., Zhang, H., Martineau, R.C., Zhao, H., Zou, L., Andrs, D., Hansel, J., 2018. Relap-7 theory manual. Tech. rep., Idaho National Lab.(INL), Idaho Falls, ID (United States).
- Black, G., Shropshire, D., Araújo, K., van Heek, A., 2022. Prospects for nuclear microreactors: A review of the technology, economics, and regulatory considerations. Nucl. Technol. 1–20.
- Brockmeyer, L., Merzari, E., Solberg, J., Hassan, Y., 2020. One-way coupled simulation of FIV in a 7-pin wire-wrapped fuel pin bundle. Nucl. Eng. Des. 356, 110367.
- Chiew, Y., Glandt, E., 1983. The effect of structure on the conductivity of a dispersion. J. Colloid Interface Sci. 94 (1), 90–104.

- Electric Power Research Institute, 2019. Uranium oxycarbide (UCO) tristructural isotropic (TRISO) coated particle fuel performance. EPRI-AR-1 (NP).
- Folsom, C., Xing, C., Jensen, C., Ban, H., Marshall, D.W., 2015. Experimental measurement and numerical modeling of the effective thermal conductivity of TRISO fuel compacts. *J. Nucl. Mater.* 458, 198–205.
- Gaspar, L.M., Giordano, D.A., Greenfield, N.A., Kim, S.J., Kubic, F.A., Middlemas, M.R., Pizarro, A.J., Saeger, W.J., Sweetland, K.M., Reid, R.S., 2022. eBlock37 microreactor electrical demonstration unit. *Nucl. Technol.* 1–19.
- Geuzaine, C., Remacle, J.-F., 2009. Gmsh: A 3-D finite element mesh generator with built-in pre-and post-processing facilities. *Internat. J. Numer. Methods Engrg.* 79 (11), 1309–1331.
- Gonzo, E.E., 2002. Estimating correlations for the effective thermal conductivity of granular materials. *Chem. Eng. J.* 90 (3), 299–302.
- Guo, Y., Li, Z., Wang, K., Su, Z., 2022. A transient multiphysics coupling method based on OpenFOAM for heat pipe cooled reactors. *Sci. China Technol. Sci.* 65 (1), 102–114.
- Hales, J., Novascone, S., Spencer, B., Williamson, R., Pastore, G., Perez, D., 2014. Verification of the BISON fuel performance code. *Ann. Nucl. Energy* 71, 81–90.
- Hollrah, B., Zou, L., Filippone, C., 2022. Preliminary thermal-hydraulics and selected safety analysis for holos-quad reactor design. Tech. rep., Argonne National Lab.(ANL), Argonne, IL (United States).
- Hu, G., Hu, R., Zou, L., 2019. Development of heat pipe reactor modeling in sam. Tech. rep., Argonne National Lab.(ANL), Argonne, IL (United States).
- Im, J., Jeong, M.J., Choi, N., Kim, K.M., Cho, H.K., Joo, H.G., 2023. Multiphysics analysis system for heat pipe cooled micro reactors employing PRAGMA-OpenFOAM-ANLHTP. *Nucl. Sci. Eng.* 1–15.
- Jin Jeong, M., Lee, S., Kyu Cho, H., 2022. Verification and validation of the OpenFOAM stress analysis solver for heat pipe cooled micro reactor simulation. In: 19-th International Topical Meeting on Nuclear Reactor Thermal Hydraulics.
- Leppänen, J., Pusa, M., Viitanen, T., Valtavirta, V., Kaltiaisenaho, T., 2015. The Serpent Monte Carlo code: Status, development and applications in 2013. *Ann. Nucl. Energy* 82, 142–150.
- Lindsay, A.D., Gaston, D.R., Permann, C.J., Miller, J.M., Andrš, D., Slaughter, A.E., Kong, F., Hansel, J., Carlsen, R.W., Icenhour, C., et al., 2022. 2.0-MOOSE: Enabling massively parallel multiphysics simulation. *SoftwareX* 20, 101202.
- Matthews, C., Laboure, V., DeHart, M., Hansel, J., Andrs, D., Wang, Y., Ortensi, J., Martineau, R.C., 2021. Coupled multiphysics simulations of heat pipe microreactors using DireWolf. *Nucl. Technol.* 207 (7), 1142–1162.
- Mueller, C., Tsvetkov, P., 2021. A review of heat-pipe modeling and simulation approaches in nuclear systems design and analysis. *Ann. Nucl. Energy* 160, 108393.
- Nabielek, H., Fukuda, K., Minato, K., Ogawa, T., 1992. Calculation of particle temperatures in NSRR tests. Tech. rep., Japanese Atomic Energy Agency.
- Panda, K., Dulera, I., Basak, A., 2017. Numerical simulation of high temperature sodium heat pipe for passive heat removal in nuclear reactors. *Nucl. Eng. Des.* 323, 376–385.
- Patankar, S.V., 2018. *Numerical Heat Transfer and Fluid Flow*. CRC Press.
- Poston, D.I., 2018. KRUSTY test results. Tech. rep., Los Alamos National Lab.(LANL), Los Alamos, NM (United States).
- Price, D., Kinast, S., Barr, K., Kochunas, B., Filippone, C., 2022a. A perturbation-based hybrid methodology for control drum worth prediction applied to the HOLOS-Quad microreactor concept. *Ann. Nucl. Energy* 168, 108903.
- Price, D., Kozlowski, T., 2021. A multiscale approach to analyze the effect of radial void fraction distributions on BWR neutronic lattice parameters. *Ann. Nucl. Energy* 152, 107988.
- Price, D., Maile, A., Peterson-Droogh, J., Blight, D., 2022b. A methodology for uncertainty quantification and sensitivity analysis for responses subject to Monte Carlo uncertainty with application to fuel plate characteristics in the ATRC. *Nucl. Eng. Technol.* 54 (3), 790–802.
- Price, D., Roskoff, N., Radaieh, M.I., Kochunas, B., 2023. Serpent-OpenFOAM coupling of an evinci motivated microreactor. In: International Conference of Mathematics and Computational Methods Applied To Nuclear Science and Engineering.
- Roskoff, N., Kucukboyaci, V., Levinsky, A., 2022a. Modeling and analysis of a micro-reactor using the DireWolf code suite. In: Proceedings of the International Conference on Physics of Reactors-PHYSOR 2022.
- Roskoff, N., Kucukboyaci, V., Levinsky, A., 2022b. Transient analysis of a micro-reactor using the DireWolf code suite. In: Proceedings of the International Conference on Physics of Reactors-PHYSOR 2022.
- Shropshire, D.E., Black, G., Araújo, K., 2021. Global market analysis of microreactors. Tech. rep., Idaho National Lab.(INL), Idaho Falls, ID (United States).
- Stainsby, R., Grief, A., Worsley, M., Dawson, F., 2009. Investigation of Local Heat Transfer Phenomena in a Pebble Bed HTGR Core. AMEC NSS Limited, London, United Kingdom.
- Stauff, N., Lee, C., Filippone, C., 2022. Core design of the holos-quad microreactor. Tech. rep., Argonne National Lab.(ANL), Argonne, IL (United States).
- Stauff, N., Lee, C., Shriwise, P., Miao, Y., Hu, R., Vegendla, P., Fei, T., 2019. Neutronic design and analysis of the holos-quad concept. Tech. rep., Argonne National Lab.(ANL), Argonne, IL (United States).
- Swartz, M.M., Byers, W.A., Lojek, J., Blunt, R., 2021. Westinghouse evinci™ heat pipe micro reactor technology development. In: International Conference on Nuclear Engineering. Vol. 85246, American Society of Mechanical Engineers, V001T04A018.
- Sweet, J., Roth, E., Moss, M., 1987. Thermal conductivity of Inconel 718 and 304 stainless steel. *Int. J. Thermophys.* 8 (5), 593–606.
- Testoni, R., Bersano, A., Segantini, S., 2021. Review of nuclear microreactors: Status, potentialities and challenges. *Prog. Nucl. Energy* 138, 103822.
- Wang, C., Chen, J., Qiu, S., Tian, W., Zhang, D., Su, G., 2017. Performance analysis of heat pipe radiator unit for space nuclear power reactor. *Ann. Nucl. Energy* 103, 74–84.
- Zuo, Z., Faghri, A., 1998. A network thermodynamic analysis of the heat pipe. *Int. J. Heat Mass Transfer* 41 (11), 1473–1484.